The impact of advection schemes on lateral shear and baroclinic instability

Mahdi Mohammadi-Aragh[a,1], Knut Klingbeil[a], Nils Brüggemann[b], Carsten Eden[b], Hans Burchard[a,*]

[a] *Leibniz Institute for Baltic Sea Research Warnemünde, Seestraße 15, D-18119 Rostock, Germany*
[b] *Institute of Oceanography, University of Hamburg, Bundesstraße 53, D-20146 Hamburg, Germany*

Abstract

This paper quantifies spurious dissipation and mixing of various advection schemes in idealized experiments of lateral shear and baroclinic instabilities in numerical simulations of a re-entrant Eady channel for configurations with large and small Rossby numbers. Effects of advection schemes on the evolution of background potential energy and the dynamics of the restratification process are analysed. The advection schemes for momentum and tracer are considered using several different methods including a recently developed local dissipation analysis. We use the Weighted Essentially Non-Oscillatory (WENO) scheme and the 5-point-stencil Monotonicity Preserving (MP5) scheme as highly accurate but complex schemes. As lower order, less complex schemes, we use Total Variation Diminishing (TVD) schemes, e.g. the Symmetric Piecewise-Linear (SPL-max-$\frac{1}{3}$) scheme and a Third-Order-Upwind scheme. The analysis shows that the MP5 and SPL-max-$\frac{1}{3}$ schemes provide the best results with MP5 being approximately 2.3 times more expensive in our implementation. In contrast to the configuration with a small Rossby number, when significant differences between schemes become apparent, the different advection schemes behave similarly for a larger Rossby number. Another major outcome of the present study is that generally positive global numerical dissipation and positive background potential energy evolution delay the restratification process.

Keywords: Numerical dissipation, numerical mixing, mesoscale, submesoscale, baroclinic instability, lateral shear instability, numerical viscosity, numerical diffusivity, advection scheme, WENO, MP5, TVD

1. Introduction

It is well known that truncation errors of the discretised advection terms lead to spurious mixing and dissipation and may interact nonlinearly with parameterisations of turbulent mixing and transport. Hecht (2010), for example, attributes spurious cooling within and below the thermocline to interactions between dispersive centered tracer advection schemes and eddy parameterisations. Holland et al. (1998) discuss the

*Corresponding author.
Email address: hans.burchard@io-warnemuende.de (Hans Burchard)
[1] Now at: *Alfred Wegener Institute, Helmholtz Centre for Polar and Marine Research, P.O. Box 12 01 61, D-27515 Bremerhaven, Germany. Email address:* maragh@awi.de (Mahdi Mohammadi-Aragh)

local Gibbs phenomenon in the light of local anomalies due to overshooting and undershooting oscillations in the tracer field. Farrow and Stevens (1995) find unphysical negative surface temperature and spurious heating in some regions of an eddying Antarctic model. Griffies et al. (2000) suggest minimizing the amount of spurious diapycnal mixing in the oceans pycnocline by properly resolving the admitted scales of motion. Lee et al. (2002) report excessive effective diffusion due to numerical mixing and suggest using less diffusive horizontal advection schemes and appropriate vertical resolution. These numerical inaccuracies are a major factor hampering the representation of eddy transport and eddy-mean flow interaction in baroclinic instabilities and lateral shear instabilities.

In ocean modelling, the main attempts to remove the stability problems with the simple central advection schemes have been to use more diffusive schemes. Holland et al. (1998), for example, discuss a simulation with a physically more realistic tracer pattern in a global model by using upstream schemes instead of central advection schemes. Some methods that deal with the control of generation of spurious anomalies are now widely implemented in ocean modelling. The Flux Limiter Method (FLM; Sweby, 1984), the Flux-Corrected Transport (FCT) algorithm (Boris and Book, 1973; Zalesak, 1979) and the Piecewise Parabolic Method (PPM; Colella and Woodward, 1984) are examples. Notwithstanding the substantial progress, these schemes often suffer from diffusive or antidiffusive effects. Diffusive schemes cause energy loss in ocean models due to discrete variance decay of tracer and momentum, in contrast antidiffusive schemes add energy to the system. The former tends to slow down oceanic processes like baroclinic instability and the latter accelerates them nonphysically. It is expected that the high accurate advection schemes minimize these problems by more accurately simulating the discontinuities and maxima in the tracer and momentum field and will reduce the unwanted variance decay.

Due to the lack of analytical solutions, the quantification of truncation errors is difficult in complex three-dimensional model simulations. Fringer and Armfield (2005) further developed the idea of background potential energy originally proposed by Winters et al. (1995) and Winters and D'Asaro (1996) and suggest estimating the spurious diapycnal mixing from the variations in the background potential energy. Following this approach, Getzlaff et al. (2010) compute effective diffusivities and Ilıcak et al. (2012) quantify the global spurious dianeutral transport. Urakawa and Hasumi (2014) quantify numerical mixing in terms of spurious water mass transformation rates. A different approach is taken by Burchard and Rennau (2008), inspired by the work of Morales Maqueda and Holloway (2006), to quantify local numerical mixing in terms of the local tracer variance decay induced by the advection scheme. This is generalized to a similar approach to quantify numerical dissipation as a kinetic energy loss due to the discretisation of the momentum advection (see Burchard (2012) and Klingbeil et al. (2014)). In this paper the energy variation due to both numerical dissipation for the momentum equations and numerical mixing for the tracer equation is investigated using the numerical dissipation analysis of Klingbeil et al. (2014) as well as the background potential energy analysis by Winters et al. (1995).

Despite the progress in developing the diagnostic methods of numerical mixing and dissipation, all the studies reviewed so far, however, did not study systematically the behaviour of advection schemes in oceanic applications. This motivated us to investigate these effects in a specific ocean model (General Estuarine Transport Model; Burchard and Bolding, 2002). Since all sources of energy loss in the ocean model are the same for all analyses, and only the deployed advection scheme is changed, all numerical effects are directly related to the used advection schemes. We also expect that the advection schemes behave qualitatively similar in other ocean models. In addition, we want to answer the question whether the high accurate advection schemes used in engineering applications can also provide better predictability for ocean models. For this purpose the Weighted Essentially Non-Oscillatory (WENO) scheme (Liu et al., 1994) and the 5-point-stencil Monotonicity Preserving (MP5) advection scheme (Suresh and Huynh, 1997) are compared with the flux limiter advection schemes.

We apply the diagnosis of numerical dissipation and mixing to idealized re-entrant channel simulations of lateral and baroclinic shear instability under different dynamical conditions. Such configurations are also used to develop and test eddy parameterisations (Fox-Kemper et al., 2008; Brüggemann and Eden, 2014). Since we expect that such instability processes suffer from the discretisation errors of both momentum and tracer advection schemes, the advection schemes are initially categorised based on their dissipative behaviour in a test case of lateral shear instability. Then, in the baroclinic instability experiment, we verify the effects of different momentum and tracer advection schemes on the generation of eddies. For all setups the WENO and MP5 schemes are compared to popular TVD schemes and the simple Third-Order-Upwind scheme (see Table 1 for detail).

2. Ocean model and methodology

In this section the main features of the advection schemes and ocean model we use are explained. Then, the methods used to investigate the effects of discretisation errors of advection schemes are introduced.

2.1. Advection schemes

The simplest possible discretisation of the advection equation e.g., First Order Upwind (FOU), is highly diffusive and consequently useless for long-term unsteady simulations. However, higher order schemes, that provide higher level of accuracy than FOU, generate unacceptable oscillations near discontinuities. The most well-known approach to avoid oscillations is imposing monotonicity to the schemes to make them TVD (Total

Variation Diminishing). The Flux Limiter Method (FLM), for instance, which has been introduced by Sweby (1984), is designed such that it benefits from the monotonicity of a first order scheme and adopts nonlinearity properties of higher order schemes. The reader is referred to Thuburn (1997) for the similarity between TVD-schemes and Positive Schemes and Berger et al. (2005) and Spekreijse (1987) for similarities between slope limiters and FLM. These schemes often suffer from some issues such as smearing and squaring effects near discontinuities and maxima, see e.g. Čada and Torrilhon (2009). These effects cause both numerical dissipation and antidissipation in oceanic applications. The WENO scheme, as an example, aims to minimize these problems by using a convex combination of all possible stencils for computing the interfacial value providing higher-order accuracy in smooth regions and seeking the smoothest solution near discontinuities. The MP5 scheme employs a five-point stencil in a complex geometric approach to approximate the advective flux. One aim of this paper is to compare the effects of these two more recent schemes with the more established flux-limited schemes.

2.2. Ocean model

We use the General Estuarine Transport Model (GETM, www.getm.eu, for details see Burchard and Bolding (2002); Hofmeister et al. (2010); Klingbeil and Burchard (2013)). GETM is a primitive-equation, finite-volume, structured-grid model on an Arakawa C-grid, with bottom- and surface-following general vertical coordinates and explicit mode-splitting into a vertically integrated barotropic mode and a vertically resolved baroclinic mode. Several advection schemes for momentum and tracers which are solved in a flux form are implemented as directional-split schemes. In our simulations a linear version of the equation of state is used. The model has mainly been applied to coastal (Banas et al. (2007); Hofmeister et al. (2013)), estuarine (Burchard et al. (2004); Burchard et al. (2011)), shelf sea (van Leeuwen et al. (2013); Holtermann et al. (2014)) and lake (Umlauf and Lemmin (2005); Becherer and Umlauf (2011)) applications.

2.3. Methodology

The variation of the energy level in the system due to numerical mixing and numerical dissipation is diagnosed using the background potential energy (see e.g. Fringer and Armfield (2005)) and numerical dissipation analysis of Klingbeil et al. (2014), respectively. The effects of advection schemes on the dynamics of the flow are also investigated using eddy kinetic energy and potential energy anomaly time series.

Background potential energy (BPE)

Background potential energy,

$$BPE = g \int_V \rho(z_*(\mathbf{x},t)) z_*(\mathbf{x},t) \ \mathrm{d}V, \tag{1}$$

is defined here as the lowest level of potential energy of the system after an adiabatic rearrangement (Winters et al., 1995). In the above relation $\rho(z_*(\mathbf{x},t))$ and $z_*(\mathbf{x},t)$ denote the density of the stably stratified sorted fluid and the height of the fluid parcel at position $(\mathbf{x},t)$ from a reference level after the rearrangement. The background potential energy remains constant if there is no mixing of temperature and salinity. However, even in the absence of physically induced mixing, numerical diapycnal fluxes change the background potential energy. Following the work of Winters et al. (1995) and Winters and D'Asaro (1996), Griffies et al. (2000) quantify the rate of numerical diapycnal mixing empirically by diagnosing the effective diffusivity from

$$k_{\text{eff}}\left(z_*\left(\mathbf{x},t\right)\right) = \frac{-F\left(z_*\left(\mathbf{x},t\right)\right)}{\partial_{z_*(\mathbf{x},t)}\rho\left(z_*\left(\mathbf{x},t\right)\right)} \tag{2}$$

where the averaged diapycnal flux $F\left(z_*\left(\mathbf{x},t\right)\right)$ is computed as

$$F\left(z_*\left(\mathbf{x},t\right)\right) = \frac{1}{A}\int \boldsymbol{F_D}\ .\hat{\boldsymbol{\rho}}\ \mathrm{d}S \tag{3}$$

In (2) and (3), A, dS, $\hat{\boldsymbol{\rho}}$ and $\boldsymbol{F_D}$ are horizontal cross-sectional area of the fluid domain, the differential area element for an isopycnal surface, a diapycnal unit vector and the amount of flux crossing an isopycnal surface, respectively. For the comparison of the effects of advection schemes the vertically averaged effective diffusivity,

$$k_{\text{avg}}^{\text{num}} = \frac{\int |k_{eff}(z_*\left(\mathbf{x},t\right))|\ \mathrm{d}z_*\left(\mathbf{x},t\right)}{\int\ \mathrm{d}z_*\left(\mathbf{x},t\right)} \tag{4}$$

is computed as a single number.

Numerical dissipation

The conservation of discrete energy in numerical models is the focus of several studies, see e.g. Arakawa (1966), Marsaleix et al. (2008) and Klingbeil et al. (2014). These authors show that significant loss of kinetic energy is caused by truncation errors associated with the numerical advection of discrete momentum. Klingbeil et al. (2014) develop a 3D analysis method to quantify this spurious (numerical) dissipation in each grid cell. Their analysis follows Burchard and Rennau (2008), labelled there as BR08, and is based on the variance decay of the single velocity components $\left(\chi^u_{i+1/2,j,k}, \chi^v_{i,j+1/2,k}, \chi^w_{i,j,k+1/2}\right)$ and diagnoses for the C-grid a local numerical dissipation rate

$$\frac{1}{2}\chi_d\left(\mathbf{u}\right)_{i,j,k} = \frac{1}{\mathrm{d}V_{i,j,k}}\left(\chi_i + \chi_j + \chi_k\right), \tag{5}$$

where

$$\chi_i = \frac{1}{2}\left(\mathrm{d}V_{i-1/2,j,k}\left(\frac{1}{2}\chi^u_{i-1/2,j,k}\right) + \mathrm{d}V_{i+1/2,j,k}\left(\frac{1}{2}\chi^u_{i+1/2,j,k}\right)\right), \tag{6}$$

$$\chi_j = \frac{1}{2}\left(\mathrm{d}V_{i,j-1/2,k}\left(\frac{1}{2}\chi^v_{i,j-1/2,k}\right) + \mathrm{d}V_{i,j+1/2,k}\left(\frac{1}{2}\chi^v_{i,j+1/2,k}\right)\right), \tag{7}$$

$$\chi_k = \frac{1}{2}\left(\mathrm{d}V_{i,j,k+1/2}\left(\frac{1}{2}\chi^w_{i,j,k-1/2}\right) + \mathrm{d}V_{i,j,k+1/2}\left(\frac{1}{2}\chi^w_{i,j,k+1/2}\right)\right), \tag{8}$$

where

$$\chi^u_{i+1/2,j,k} = \frac{\mathcal{ADV}\left\{u^2\right\}_{i+1/2,j,k} - \left(\mathcal{ADV}\left\{u\right\}_{i+1/2,j,k}\right)^2}{\triangle t} \tag{9}$$

and $\mathcal{ADV}$ is the advection operator.

The accumulated global numerically dissipated energy is then:

$$ND = \int\int \frac{1}{2}\chi_d\left(\mathbf{u}\right)_{i,j,k}\rho_0 \text{ d}V \text{ d}t. \tag{10}$$

The local and global numerical (kinematic) viscosity are also diagnosed. For the 2D lateral shear instability experiment (section 3), local and global numerical viscosity ($\nu^{\mathrm{h}}_{\mathrm{num}}$ and $\nu^{\mathrm{h}}_{\mathrm{num,g}}$, respectively) associated with the depth-integrated momentum equations are given by

$$\nu^{\mathrm{h}}_{\mathrm{num}} = \frac{\chi\left(\mathbf{u}\right)}{2S_{\alpha\beta}S_{\alpha\beta}}, \tag{11a}$$

$$\nu^{\mathrm{h}}_{\mathrm{num,g}} = \frac{\int\chi\left(\mathbf{u}\right)\rho_0\mathrm{d}V}{\int 2S_{\alpha\beta}S_{\alpha\beta}\rho_0\mathrm{d}V}, \tag{11b}$$

with the lateral rate of strain $S_{\alpha\beta} = \frac{1}{2}\left(\partial_\alpha u_\beta + \partial_\beta u_\alpha\right)$ and $\alpha, \beta \in \{\mathrm{x},\mathrm{y}\}$. This diagnostic is only used for the 2D lateral shear instability experiment for which the local numerical viscosity can be considered to be isotropic.

Eddy kinetic energy and available potential energy

Differences in the total eddy kinetic energy, the difference between total and mean kinetic energy,

$$EKE = \frac{1}{2}\int\left((u-\hat{u})^2 + (v-\hat{v})^2 + (w-\hat{w})^2\right)dV \tag{12}$$

show the influence of advection schemes on the eddy field. In (12), $\hat{u}$, $\hat{v}$ and $\hat{w}$ are zonally-averaged velocity components. In addition, available potential energy can quantify indirectly the stratification of the fluid. Available potential energy $APE = PE - BPE$, is computed as the difference between potential energy

$$PE = g\int_V \rho(z(\mathbf{x},t))z(\mathbf{x},t) \text{ d}V, \tag{13}$$

and BPE, derived in (1).

Diapycnal diffusivity

In order to evaluate different parameterisations for eddy fluxes, Brüggemann and Eden (2014) evaluate the diapycnal diffusivity

$$k_{dia} = -\frac{\overline{v'b'}\partial_y\overline{b} + \overline{w'b'}\partial_z\overline{b}}{|\nabla\overline{b}|^2}, \tag{14}$$

where the diagnosed $\overline{v'b'}$ and $\overline{w'b'}$ are computed by considering the zonal and time mean of the velocity components $(\overline{v}, \overline{w})$ and buoyancy $\overline{b}$ and corresponding deviations denoted by $(\ )'$. The dependency of the diapycnal diffusivity profile on the different advection schemes is investigated in this study. Note that rotational eddy fluxes can bias k_{dia} if calculated in accordance to Eq. (14) (see Eden et al. (2007)). However, we assume that rotational eddy fluxes do not significantly influence k_{dia} calculated after Eq. (14) and we omit a more complicated derivation.

3. Lateral shear instability experiment

The lateral shear instability problem is designed as a zonal jet representative of for instance the Gulf stream. Instability is studied using the depth-integrated barotropic mode of GETM in Cartesian coordinates with an f-plane approximation with the Coriolis parameter $f_0 = 8.36 \times 10^{-5} s^{-1}$ in a zonal, flat bottom re-entrant channel of 1000 m depth and 240 km width. Since explicit viscosity is not employed in the model, all dissipation is due to the numerics. The simulations are conducted for the three horizontal resolutions of 5 km, 2.5 km and 1.25 km. Since the high resolution configuration of the experiment generates the least numerical dissipation, the results of the highest-resolution simulation using the MP5 advection scheme are considered as reference. The experiment is configured for two different types of zonal velocity distribution. The first case (Eq. 15), hereafter GaussJet, is a jet with double exponential meridional distribution of zonal velocity and the velocity profile of the second case (Eq. 16), hereafter BoxJet, is combination of a box and a point jet (concentration of vorticity at a single point),

$$u^{\text{GaussJet}}(y) = u_{\max} exp[\frac{-(y-y_c)^2}{2\sigma^2}] \tag{15}$$

$$u^{\text{BoxJet}}(y) = \begin{cases} 0, & y < y_1 \\ u_{\max} - u_{\text{box}} \frac{|y-y_{\text{c}}|}{y_2 - y_{\text{c}}}, & y_1 \leq y \leq y_2, \\ 0, & y > y_2 \end{cases} \tag{16}$$

In the above relation, y is the meridional distance from the southern solid boundary, and we choose $\sigma = 9$ km, $u_{\max} = 2.5$ m s^{-1}, $u_{\text{box}} = 2.0$ m s^{-1}, $y_{\text{c}} = L_y/2$, $y_1 = L_y/4$, $y_2 = 3L_y/4$ where $L_y = L_{\text{x}} = 240$ km denotes the width and length of the channel (see Figure 1). The velocity profiles of both cases include at least two Rayleigh inflection points that satisfy the necessary condition for instability (Vallis, 2006). The geostrophically adjusted surface elevation η, which is computed numerically using the initial zonal velocity, is perturbed to generate lateral shear instability. Small perturbations grow and evolve into much larger ones. This process causes an exchange of energy between mean and eddy energy. Eddies are then dissipated due to numerical dissipation.

Figure 2 shows the evolution of the vorticity field for both jet configurations using the high resolution simulation and the MP5 scheme. The initial perturbations are amplified by extracting energy from the background flow and potential energy. Then, unstable vortices are generated which finally evolve into much larger ones. This process causes an exchange of energy between potential energy and kinetic energy and between the background velocity field and eddies. Total energy will be gradually dissipated by numerical dissipation. Figure 2 shows that the point jet in the initial velocity field in BoxJet has made the flow more stable to the perturbation in comparison to GaussJet. Thus, the outset of vortical dynamics in GaussJet is earlier than BoxJet. In addition, the existing initial sharp discontinuities in the velocity field in BoxJet causes the generation of eddies with smaller spatial scales than eddies emerged in GaussJet.

Figure 3a compares time series of numerical dissipation for the lowest resolution configuration in GaussJet with the reference case. The high resolution set-up of GaussJet is chosen as the reference since it generates the least numerical dissipation (see Table 2). In addition, increasing the resolution from 1.25 km to 0.625 km does not increase the eddy kinetic energy level (see Figure 3b), which shows that the contribution of the new resolved turbulent flow to the eddy kinetic energy level and numerical dissipation is insignificant. The results presented in figure 3a demonstrate that the Superbee and SPL-$\frac{1}{3}$ advection schemes show significant antidissipative and dissipative behaviour, respectively. The different dissipative behavior is due to the fact that the flux limiter methods (e.g. Superbee, SPL-$\frac{1}{3}$), in contrast to the MP5 and WENO schemes that always use higher-order polynomials to compute the interfacial value, increase the proportion of the first-order upwind advection scheme in the solution to guarantee monotonicity and consequently damp the numerical oscillation. This dissipates kinetic energy numerically. However later, the results demonstrate that for some flux-limiter schemes when the sharp gradients are smoothed, the kinetic energy is increased again due to a reduced contribution of the upwind scheme. These schemes introduce edges to the solution (see e.g. Čada and Torrilhon, 2009), which adds kinetic energy to the system or intensifies the buoyancy gradients numerically. Figure 3b compares the total eddy kinetic energy of GaussJet. For GaussJet, low-resolution simulations with WENO, MP5 and SPL-max-$\frac{1}{3}$ schemes generate similar eddy kinetic energy as in the reference MP5 simulation. However, for BoxJet (not shown), the higher resolution reference simulation (using the MP5 scheme) resolves more eddies and generates a higher level of eddy kinetic energy. The maximum difference between the final EKE for both cases and the low resolution configuration is approximately 20 percent of initial mechanical energy. Figures 3c and 3d show that the dissipative schemes (e.g. SPL-$\frac{1}{3}$) generate positive and the antidissipative scheme (Superbee) generates negative global numerical viscosity while MP5 and SPL-max-$\frac{1}{3}$ (neutral schemes) generate a relatively small global numerical viscosity. In addition, the global numerical viscosity of the Superbee scheme in BoxJet is slightly positive in the earlier stage of instability where sharp velocity gradients still exist.

Figures 4a and 4b compare two snapshots of local numerical dissipation rate of the GaussJet for the Superbee and SPL-$\frac{1}{3}$ schemes. The comparison demonstrates that Superbee has the largest area of negative values and SPL-$\frac{1}{3}$ is mostly positive which explains the global negative and positive numerical dissipation of the Superbee and SPL-max-$\frac{1}{3}$ schemes. When the antidissipative schemes, e.g. the Superbee scheme, generate globally negative numerical dissipation rates, the regions with high negative numerical dissipation rate are larger than the areas with the positive values. Figure 4c shows the snapshot of local numerical viscosity of the GaussJet using (11a). The local numerical viscosity includes regions with positive and negative local values. The results demonstrate that the regions with the high magnitude of local numerical viscosity coincide with high numerical dissipation rate. However, this does not always apply since the regions with very small magnitude of shear have high numerical viscosity too. Following the approach that Ilıcak et al. (2012) used to show the relation of the grid Reynolds number to the rate of change of background potential energy, the grid Reynolds number is shown here locally and to compare with the local numerical dissipation. Figure 4d shows the grid Reynolds numbers which are computed using the local horizontal velocity and local numerical viscosity. The results indicate that in contrast to the conclusion of Ilıcak et al. (2012) that high tracer diffusion is associated with high Reynolds numbers, here regions with high dissipation rate show low Reynolds numbers. This relation also follows when computing a Reynolds number using the global numerical viscosity and the maximum initial velocity. Using the global numerical viscosity of different advection schemes for both GaussJet and BoxJet shown in Figs. 3c and 3d and considering the constant initial velocity as the velocity scale, the relation of high (anti-)dissipative schemes generating low Reynolds numbers is reconfirmed. However, this relation might not be correct for the regions with very low shear. Since refining the grid reduces the global numerical viscosity, the grid Reynolds number will also be increased.

Table 2 compares the ratio of the total accumulated numerically dissipated energy to the total initial mechanical energy for the three resolutions for all advection schemes. For both cases increasing the resolution reduces the numerical dissipation. As expected, the FOU advection scheme shows the highest amount of dissipation. In addition, Superbee and SPL-$\frac{1}{3}$ have the highest negative and positive numerical dissipation among the TVD schemes. SPL-max-$\frac{1}{3}$ and MP5 generate the least absolute dissipation. The amount of dissipation for the Third-Order-Upwind scheme for the high resolution experiment is comparable to the WENO and MP5 schemes.

4. Baroclinic instability experiment

We use an eddying channel flow experiment to diagnose the effects of numerical mixing and dissipation on baroclinic instabilities. Such configurations are often used to validate mixing parameterisations (e.g., Fox-Kemper et al., 2008; Eden, 2010, 2011; Skyllingstad and Samelson, 2012). Our configuration resembles the models of Eady (1949) and Stone (1966) (see Brüggemann and Eden (2014) for more details).

The configuration is a zonal, re-entrant, flat-bottom channel on a f-plane. There is a constant vertical and meridional buoyancy gradient and a zonal background velocity in thermal wind balance which is unstable to small perturbations. The northern and southern solid boundaries are considered as free slip. Similar to the lateral shear instability experiment, explicit viscosity and diffusivity are not employed in the model. Note that the same advection schemes for all spatial directions are selected for the momentum and tracer equation. However, due to the fact that MP5 and WENO schemes are very expensive algorithms they are selected here only for the horizontal direction. For this simulation scenario, the vertical advection scheme of P2-PDM is applied together with the schemes of WENO and MP5 for both tracer and momentum equations. For another scenario, the Third-Order-Upwind scheme is also used for the momentum equations for all directions and in combination with the P2-PDM scheme for the tracer equation. In addition to these simulations, another series of simulations is also performed. In these simulations one advection scheme is used for the momentum equations in all directions while the advection schemes for the tracer is changed. The results of these simulations show similar diffusive effects for the tracer field. However, the diffusive schemes used for the tracer equations provide less kinetic energy for the momentum advection scheme to dissipate. Less numerical dissipation due to diffusive tracer advection is demonstrated and explained by Klingbeil et al. (2014)

The configurations differ in their horizontal grid sizes and dynamical regimes, namely with Rossby numbers of 0.1 and 0.8, respectively (see Table 3). The grid sizes for the setups N32, N64, N128, N256 for the configuration with $Ro = 0.8$ are 5 km, 2.5 km, 1.25 km and 0.625 km and for the configuration with $Ro = 0.1$ are 40.0 km, 20.0 km, 10.0 km and 5.0 km, respectively. Small perturbations are added to the temperature field which grow continuously until finite amplitude baroclinic waves develop (Figures 5a and 6a). In this stage, the re-stratification process is initiated (Figures 5b and 6b). The zonal scale of the fastest growing modes, L_s, using the classical Eady solution for the configuration with $Ro = 0.1$ and Stone's approximation for finite Richardson numbers Ri for the configuration with $Ro = 0.8$ are approximated as $L_s \approx 3.9$ km and $L_s = 2\pi/k_s \approx 25.175$ km, respectively. k_s is computed as

$$k_s = \sqrt{\frac{5/2}{1+Ri}}\frac{f}{U_0} \tag{17}$$

where U_0 and R_i are 0.2 m s^{-1} and 1.562, respectively. In (17), k_s and U_0 are wavenumber and velocity scale, respectively. At the phase that finite amplitude baroclinic waves are developed, the computed scale of maximum instability based on spectral analysis of velocity field, in good agreement with the approximations, are 155 km and 25 km for the configurations with $Ro = 0.1$ and $Ro = 0.8$, respectively. Growth of the unstable waves (see Figures 5c and 6c) is driven by a conversion of available potential energy into eddy kinetic energy. In this stage, the restratification process is intensified (see Figures 5d and 6d). Later, the fluid is almost stratified (see Figures 5f and 6f) and closed asymmetric eddies and symmetric dipoles emerge for the configurations with low and high Rossby numbers, respectively (see Figures 5e and 6e).

In the rest of this section the effects of the advection schemes on the components of total energy are analysed. Figure 7 explains the components of the total energy and their evolution in the baroclinic instability. The initial background potential energy is considered as reference while the sum of the initial available potential energy and the initial kinetic energy are considered as the initial mechanical energy. Eddy kinetic energy extracts energy from available potential energy and accelerates the mean kinetic energy. When the flow is almost stratified, energy is exchanged between eddy kinetic energy and mean kinetic energy. This phase is associated with shear production of eddies and reduction of numerical dissipation rate and background potential energy variation. In addition to the dissipation of kinetic energy other sources of numerical errors contribute in energy lost (Tartinville et al. (1998), important ones are grid-staggering and internal pressure gradient errors which contribute to the residual in our energy budget).

4.1. Background potential energy

Figures 8a and 8b compare the time evolution of background potential energy (BPE) for the setups with $Ro = 0.1$ and $Ro = 0.8$, respectively. They show that a larger portion of available potential energy (APE) is dissipated in the configuration with $Ro = 0.1$ than for the configuration with $Ro = 0.8$. SPL-$\frac{1}{3}$, for example, dissipates 5 percent of initial mechanical energy for the configuration with $Ro = 0.8$ and 10 percent for the configuration with $Ro = 0.1$, respectively. Figures 8c and 8d compare the BPE of the model for all four resolutions for both configurations when approximately 70 and 65 percent of APE is released, respectively. They show that refining the grid generally decreases the BPE. They also show that all advection schemes dissipate energy globally in the restratification phase. From the outset of the simulation until approximately day 40 for the configuration with $Ro = 0.8$ and day 200 for the configuration with $Ro = 0.1$, the instability restratifies the fluid. During this phase the initial sharp temperature gradients are smoothed and all advection schemes present globally diffusive behaviour, as already seen in BoxJet of the lateral shear instability setup (see Figure 3d), where all schemes are dissipative initially. After that stage, which coincides with the threshold of switching from the initial semi-3D flow to a two-dimensional flow including eddies of larger size, the horizontal temperature gradients are weak, and the vertical heat flux is decreased. Consequently, the advection schemes are less diffusive in the second phase. In all configurations, SPL-$\frac{1}{3}$ and Superbee are the most diffusive and antidiffusive schemes, respectively.

Figures 9a and 9b compare the averaged numerical diapycnal diffusivity $k_{\text{avg}}^{\text{num}}$ of some advetcion schemes for the setup N128. It becomes evident that the most diffusive advection schemes result in the largest effective diffusivity. In addition, the averaged numerical diapycnal diffusivity of different advection schemes in the configuration with $Ro = 0.1$ are clearly distinct. In contrast, the results show that almost all advection schemes are in the same order diffusive in the restratification phase for the configuration with $Ro = 0.8$. In all configurations, SPL-$\frac{1}{3}$ and Superbee are the most diffusive and antidiffusive schemes, respectively.

Figures 9c and 9d compare the maximum averaged numerical diapycnal diffusivity of different advection schemes computed for the three different horizontal resolutions. Refining the grids decreases the maximum averaged numerical diapycnal diffusivity in the configuration with $Ro = 0.1$. In contrast, refining the grid *increases* the maximum averaged numerical diapycnal diffusivity for the configuration with $Ro = 0.8$. A possible explanation for this is that the eddies in the resolutions with $\frac{\Delta x}{L_0}$ smaller than 0.5 are properly resolved. Thus, increasing the resolution not necessarily decreases the effective diffusivity.

4.2. Numerical dissipation

Figures 10a and 10b compare the (accumulated) global numerically dissipated energy of the configurations with $Ro = 0.1$ and $Ro = 0.8$, respectively. The analyses demonstrate that the numerical dissipation evolves in two phases. The first phase is during the restratification process which causes the highest level of dissipation, and the second phase is associated with a quasi two-dimensional flow. All advection schemes in the first phase are globally dissipative. In the first phase all schemes have locally positive numerical dissipation rates. However, in the second phase, when the momentum gradients are smooth, the antidissipative schemes have a larger area of negative local numerical dissipation rate than in the first stage.

In all configurations, SPL-$\frac{1}{3}$ and Superbee are the most dissipative and antidissipative schemes, respectively. The proportion of dissipated energy in both regimes is approximately in the same order except for the Third-Order upwind scheme which allows a higher level of numerical dissipation for the configuration with high Rossby number. Figures 10c and 10d compare the numerical dissipation of the model for the configurations with $Ro = 0.1$ and $Ro = 0.8$ when approximately 70 and 65 percent of APE are released, respectively. This demonstrated that increasing the horizontal resolution generally decreases the numerical dissipation.

4.3. Available potential energy

Figures 11a and 11b compare the time evolution of the APE of different advection schemes. In contrast to the configuration with $Ro = 0.8$ where the advection schemes release APE in the same order, the advection schemes for the configuration with $Ro = 0.1$ generate different results. The antidissipative schemes reduce APE more than the others for all resolutions. The Superbee scheme reduces APE the most and the difference of final APE of the Superbee scheme with the most diffusive advection scheme, SPL-$\frac{1}{3}$, is about

5 percent of total initial mechanical energy. The sensitivity analysis (see figures 12a and 12b) to the grid size demonstrates that the low resolution experiments release much less APE in the first phase than the high resolution experiments.

4.4. Eddy kinetic energy

Figures 13a and 13b compare the evolution of eddy kinetic energy for configurations with $Ro = 0.1$ and $Ro = 0.8$. The comparison of the eddy kinetic energy in the end of first phase shows that for the configuration with $Ro = 0.1$ the Superbee scheme, as the antidissipative scheme, allows for the highest level of eddy kinetic energy. It has 20 percent more eddy kinetic energy than the most dissipative scheme, SPL-$\frac{1}{3}$. The comparison of results for the configuration with $Ro = 0.8$ and the setup N128 indicates that all schemes generate a similar level of eddy kinetic energy.

4.5. Diapycnal diffusivity

Figures 14a and 14b compare the vertical profile of diapycnal diffusivity for configurations with $Ro = 0.1$ and $Ro = 0.8$. The time averaging is done for the period where 10 to 50 percent of APE is released. The results of the configuration with $Ro = 0.1$ (see figure 14a) show that the vertical structure and the magnitude of the diapycnal diffusivity largely depended on the advection schemes. The neutral advection schemes e.g. MP5, show large amplitudes of diapycnal diffusivity in the mid water depth. The schemes with more absolute numerical diffusion show less dependency of water depth on the magnitude of diapycnal diffusivity. However, the results of the configuration with $Ro = 0.8$ (see 14b) does not show a direct dependency of diapycnal diffusivity on numerical dissipation. For $Ro = 0.8$ we find much less dependency of K_{dia} on the numerical advection scheme. In these ageostrophic experiments, K_{dia} is by one order of magnitude larger than in the geostrophic experiments with $Ro = 0.1$ in accordance to the results from Brüggemann and Eden (2014). Therefore, we assume that the effects of the numerical advection scheme is overlayed by the physical dynamics.

5. Summary and discussion

This study assesses the role of diffusive and dissipative effects of various advection schemes on baroclinic and lateral shear instabilities under different dynamical conditions categorised by large and small Rossby numbers. The question was whether advection schemes which have been successfully applied on engineering scales and for one-dimensional problems can improve the predictability of eddy permitting ocean models. All advection schemes can be categorised based on their unwanted effects near discontinuities and smooth regions in one-dimensional initial value problems. Theses effects in ocean models may cause unphysical violation of energy and tracer variance conservation. Depending on whether energy decreases, increases or is almost constant, advection schemes are categorised as dissipative, anti-dissipative and neutral, respectively. Dissipative schemes are commonly used because of their numerical stability, but also anti-dissipative schemes may be numerically stable and thus useful, see e.g. Fringer and Armfield (2005); Rennau and Burchard (2009). The advection schemes applied in the present study have been selected based on their known general properties. The original WENO and MP5 schemes were selected as highly accurate and complex algorithms. The SPL-max-$\frac{1}{3}$ and P2-PDM schemes were selected as representatives of the flux limiter schemes with minimum numerical dissipation. In addition, the SPL-$\frac{1}{3}$ scheme is representative for diffusive advection schemes, along with the very diffusive and simple First-Order Upstream (FOU) scheme, whereas the Superbee scheme is known for its anti-dissipative properties. All these properties are known from idealised one-dimensional test scenarios, but their behaviour in different dynamical regimes for the ocean is unknown. The behaviour of advection schemes which are excluded here is assumed to be comparable to schemes belonging to the same category (accurate, dissipative, anti-dissipative).

In the barotropic lateral shear instability experiment we only solve the momentum equations. Two different setups of an unstable jet were designed to investigate the performance of the advection schemes in eddying simulations which are developed from initial smooth maxima and sharp gradient in the velocity field. The numerical analyses confirmed the above-mentioned dissipative behaviour of advection schemes. However, the Superbee scheme which is known as an anti-dissipative scheme presents also global dissipative behaviour in the initial phase of the instability process. This scheme, as a hybrid scheme, adds locally the dissipation of an upwind first order scheme to the model until the sharp discontinuities are smooth. In this experiment, the MP5 scheme generates the least absolute numerical dissipation. From the flux limiter schemes, the SPL-max-$\frac{1}{3}$ scheme generates the least numerical dissipation which is comparable with the numerical dissipation of the WENO scheme. The WENO, MP5 and SPL-max-$\frac{1}{3}$ schemes are categorised as neutral schemes.

To investigate the interplay between the numerical mixing of tracers and numerical kinetic energy dissipation, the barocilinc instability experiments are performed. The results show that the tracer advection schemes which increase the BPE more, provide less kinetic energy to be dissipated by the momentum advection scheme. For all advection schemes, the variation of BPE occurs in two phases. In the first phase, which is associated with baroclinic production of eddy kinetic energy, the advection schemes which are recognised as neutral schemes in the lateral shear instability experiment increase BPE by approximately 4 to 5 percent of initial mechanical energy for oth configurations with large and small Rossby number when $\Delta x/L_0 = 1/4$. However, the diffusive scheme for the configuration with $Ro = 0.1$, SPL-$\frac{1}{3}$, and the anti-diffusive scheme, Superbee, change the BPE two times more than when these schemes are used in the configuration with $Ro = 0.8$. In contrast to the first phase, in the second phase, when turbulence is fully developed, BPE is approximately constant. The same holds for the numerical dissipation. The neutral schemes dissipate approximately 15 to 20 % of the initial mechanical energy in all simulations for the same resolution. In addition, in contrast to the first phase, the kinetic energy is only weakly dissipated. In general, the numerical dissipation and mixing rates in the first phase are much larger than in the second phase and all schemes are globally dissipative in the first phase. However, for the experiments with $Ro = 0.1$ the advection schemes which are generally known as anti-diffusive schemes present partially globally anti-dissipative and anti-diffusive behaviour during the second phase. The possible reason is that both momentum and tracer gradients are sharp in the first phase and smooth in the second phase. Therefore, the local dissipation and mixing rate are mostly positive in the first phase.

It was shown that the SPL-$\frac{1}{3}$ and Superbee schemes generate the maximum and minimum numerical dissipation and background potential energy variation, respectively. The schemes with numerical dissipation being in the middle between the numerical dissipation of the most dissipative and anti-dissipative schemes can be considered as the best advection schemes. The same should hold for the variations of background potential energy. Thus, it can be concluded that the MP5 advection scheme provides the most appropriate results for both dynamical regimes. However, the WENO scheme, despite of its complex algorithm and high computational costs, appears not to be as energy conserving as the SPL-max-$\frac{1}{3}$ scheme. The P2-PDM scheme was in general more diffusive and dissipative than the SPL-max-$\frac{1}{3}$. The SPL-$\frac{1}{3}$ scheme reduces energy more than other schemes and the Superbee scheme is the one which adds energy to the system. The result shows that the scenario of using a Third-Order-Upwind scheme for the momentum and a flux limited scheme for the tracer equation as energy conservative as the SPL-max-$\frac{1}{3}$ scheme for the configuration with high Rossby number, although the Third-Order-Upwind scheme is more dissipative than the SPL-max-$\frac{1}{3}$ scheme in the lateral shear instability experiment. Thus, the final results of this scenario also depend on the selected flux limited scheme for the tracer equation.

Results demonstrate that refining the grid reduces the global numerical viscosity of the lateral shear instability experiment and the averaged numerical diffusivity of the configuration with small Ro of the baroclinic instability experiment. However, increasing the horizontal resolution in the configuration with large Ro increases the numerical diapycnal diffusivity. This might be due to the fact that the eddies are resolved appropriately for the high resolution setups. In addition, the results of the diapycnal diffusivity analysis present similar vertical profiles for all schemes. The diapycnal diffusivity analysis shows that the vertical structure of diapycnal diffusivity depends on the applied advection schemes. The vertical profile of the diapycnal diffusivity is more water depth depended when the MP5 and SPL-max-$\frac{1}{3}$ schemes are used.

The analyses of eddy kinetic and available potential energy reveal that all advection schemes for the configuration with $Ro = 0.8$ generate approximately the same level of EKE and APE. However, when the flow is quasi two-dimensional, the dissipative schemes generate less eddy kinetic energy than the anti-dissipative schemes. However, the APE analysis of the configuration with the low Rossby number demonstrates that the anti-diffusive scheme in the first phase of stratification released more potential energy than the diffusive scheme, although they finally reach to the same level of potential energy. Furthermore, for this configuration, it was shown that the anti-dissipative schemes generate the highest eddy kinetic energy in both phases. It was also shown that refining the grids for both dynamical regimes decreases the final level of APE and consequently the final level of stratification.

For assessing the trade-offs between complex advection schemes versus high-resolution simulations, a sensitivity analysis is performed using identical advection schemes in all directions and equations for three different computational grids. As a simple test scenario, an idealised test case is selected (see Klingbeil et al. (2014) for details), since it can be performed in serial mode using GETM and its physical process is comparable to the idealised test cases used in the present study. The results (see Table 4) show that computations using the MP5 and WENO schemes are about 4-6 times more expensive than using the flux limiter schemes, depending on the model resolution. The substantial changes in relative computational costs between different model resolutions are due to the different percentage of the total computational time that the calculation of the advection terms takes for the different model resolutions. In addition, the numerical simulations using MP5 and WENO schemes for the horizontal direction of the baroclinic instability test case take approximately 2.3 times longer than simulating with flux limiters in our implementation. The SPL-max-$\frac{1}{3}$ scheme causes more appropriate variation of energy in comparison to other flux limiters, and the MP5 schemes provides best energy conservation but is several times more expensive than the flux limited schemes. In addition, the results of all experiments demonstrate that refining the grid reduces the numerical dissipation and numerical mixing of tracer. These very high extra computational costs of these accurate schemes demonstrate that those are only valuable for the generation of reference solutions rather than production simulations for complex realistic ocean scenarios.

6. Conclusion

To conclude, the results of this study show that all tested advection schemes are numerically dissipative and increase the background potential energy in the restratification phase of the baroclinic instability experiment. However, when the governing flow is 2D, the Superbee advection scheme is anti-dissipative for both test cases, while the other schemes are dissipative. One major outcome of the present study is that generally positive global numerical dissipation and positive background potential energy evolution delay the restratification process. Returning to the main question of this study, it is now possible to state that MP5 and SPL-max-$\frac{1}{3}$ generate the best results, with the MP5 being computationally more demanding but more accurate. Taken together, these results suggest to use either MP5 as a high-order advection scheme or SPL-max-$\frac{1}{3}$ as a flux limited advection scheme for eddy-resolving ocean models if new mixing parameterisations are to be derived or high accuracy of the results is demanded.

Acknowledgments

This study has been carried out in the framework of the projects *Southern Ocean Mixing* (BU 1199/12, funded by the German Research Foundation) and *Reactions of small-scale and meso-scale processes in the upper ocean mixed layer to atmospheric forcing* (SOPRAN II TP 5.1, funded by the German Federal Ministry of Research and Education). We are grateful for comments by Sergey Danilov and two anonymous reviewers that improved this manuscript. The authors would like to thank Karsten Bolding (Asperup, Denmark) for maintaining the GETM project. Financial support of Knut Klingbeil has been provided by the project MOSSCO, funded by the German Federal Ministry of Research and Education (FKZ 03F0667B).

Arakawa, A., 1966. Computational design for long-term numerical integration of the equations of fluid motion: Two-dimensional incompressible flow. Part I. J. Comp. Phys. 1, 119–143.

Banas, N., Hickey, B., Newton, J., Ruesink, J., 2007. Tidal exchange, bivalve grazing, and patterns of primary production in Willapa Bay, Washington, USA. Mar. Ecol. Prog. Ser. 341, 123–139.

Becherer, J., Umlauf, L., 2011. Boundary mixing in lakes: 1. Modeling the effect of shear-induced convection. J. Geophys. Res. 116 (C10), C10017, doi:10.1029/2011JC007119.

Berger, M., Aftosmis, M. J., Murman, S. M., 2005. Analysis of slope limiters on irregular grids. In: 43rd AIAA Aerospace Sciences Meeting and Exhibit.

Boris, J. P., Book, D. L., 1973. Flux-corrected transport. I. SHASTA, A fluid transport algorithm that works. J. Comp. Phys. 11 (1), 38–69.

Brüggemann, N., Eden, C., 2014. Evaluating different parameterizations for mixed layer eddy fluxes induced by baroclinic instability. J. Phys. Oceanogr. 44, 2524–2546.

Burchard, H., 2012. Quantification of numerically induced mixing and dissipation in discretisations of shallow water equations. Int. J. Geomath. 3 (1), 51–65.

Burchard, H., Bolding, K., 2002. GETM – a general estuarine transport model. Scientific documentation. Tech. Rep. EUR 20253 EN, European Commission.

Burchard, H., Bolding, K., Villarreal, M. R., 2004. Three-dimensional modelling of estuarine turbidity maxima in a tidal estuary. Ocean Dyn. 54 (2), 250–265.

Burchard, H., Hetland, R. D., Schulz, E., Schuttelaars, H. M., 2011. Drivers of residual circulation in tidally energetic estuaries: Straight and irrotational estuaries with parabolic cross-section. J. Phys. Oceanogr. 41, 548–570.

Burchard, H., Rennau, H., 2008. Comparative quantification of physically and numerically induced mixing in ocean models. Ocean Modell. 20, 293–311.

Čada, M., Torrilhon, M., 2009. Compact third-order limiter functions for finite volume methods. J. Comp. Phys. 228 (11), 4118–4145.

Colella, P., Woodward, P. R., 1984. The piecewise parabolic method (PPM) for gas-dynamical simulations. J. Comp. Phys. 54 (1), 174–201.

Eady, E., 1949. Long waves and cyclone waves. Tellus 1 (3), 33–52.

Eden, C., 2010. Parameterising meso-scale eddy momentum fluxes based on potential vorticity mixing and a gauge term. Ocean Modell. 32 (1), 58–71.

Eden, C., 2011. A closure for meso-scale eddy fluxes based on linear instability theory. Ocean Modell. 39 (3), 362–369.

Eden, C., Greatbatch, R. J., Olbers, D., 2007. Interpreting eddy fluxes. Journal of physical oceanography 37 (5), 1282–1296.

Farrow, D. E., Stevens, D. P., 1995. A new tracer advection scheme for Bryan and Cox type ocean general circulation models. J. Phys. Oceanogr. 25 (7), 1731–1741.

Fox-Kemper, B., Ferrari, R., Hallberg, R., 2008. Parameterization of mixed layer eddies. Part I: Theory and diagnosis. J. Phys. Oceanogr. 38 (6), 1145–1165.

Fringer, O. B., Armfield, S. W., 2005. Reducing numerical diffusion in interfacial gravity wave simulations. Int. J. Numer. Meth. Fluids 49, 301–329.

Getzlaff, J., Nurser, G., Oschlies, A., 2010. Diagnostics of diapycnal diffusivity in z-level ocean models part I: 1-Dimensional case studies. Ocean Modell. 35 (3), 173–186.

Griffies, S. M., Pacanowski, R. C., Hallberg, R. W., 2000. Spurious diapycnal mixing associated with advection in a z-coordinate ocean model. Mon. Weather Rev. 128 (3), 538–564.

Hecht, M. W., 2010. Cautionary tales of persistent accumulation of numerical error: Dispersive centered advection. Ocean Modell. 35 (3), 270–276.

Hofmeister, R., Bolding, K., Hetland, R. D., Schernewski, G., Siegel, H., Burchard, H., 2013. The dynamics of cooling water discharge in a shallow, non-tidal embayment. Cont. Shelf Res. 71, 68–77.

Hofmeister, R., Burchard, H., Beckers, J.-M., 2010. Non-uniform adaptive vertical grids for 3D numerical ocean models. Ocean Modell. 33 (1), 70–86.

Holland, W. R., Chow, J. C., Bryan, F. O., 1998. Application of a third-order upwind scheme in the NCAR ocean model. J. Clim. 11 (6), 1487–1493.

Holtermann, P., Burchard, H., Gräwe, U., Klingbeil, K., Umlauf, L., 2014. Deep-water dynamics and boundary mixing in a non-tidal stratified basin: A modeling study of the Baltic Sea. J. Geophys. Res. 119, 1465–1487.

Ilıcak, M., Adcroft, A. J., Griffies, S. M., Hallberg, R. W., 2012. Spurious dianeutral mixing and the role of momentum closure. Ocean Modell. 45, 37–58.

Klingbeil, K., Burchard, H., 2013. Implementation of a direct nonhydrostatic pressure gradient discretisation into a layered ocean model. Ocean Modell. 65, 64–77.

Klingbeil, K., Mohammadi-Aragh, M., Gräwe, U., Burchard, H., 2014. Quantification of spurious dissipation and mixing discrete variance decay in a finite-volume framework. Ocean Modell. 81, 49–64.

Lee, M.-M., Coward, A. C., Nurser, A., 2002. Spurious diapycnal mixing of the deep waters in an eddy-permitting global ocean model. J. Phys. Oceanogr. 32 (5), 1522–1535.

Liu, X.-D., Osher, S., Chan, T., 1994. Weighted essentially non-oscillatory schemes. J. Comp. Phys. 115 (1), 200–212.

Marsaleix, P., Auclair, F., Floor, J., Herrmann, M., Estournel, C., Pairaud, I., Ulses, C., 2008. Energy conservation issues in sigma-coordinate free-surface ocean models. Ocean Modell. 20, 61–89.

Morales Maqueda, M., Holloway, G., 2006. Second-order moment advection scheme applied to Arctic ocean simulation. Ocean Modell. 14 (3), 197–221.

Pietrzak, J., 1998. The use of TVD limiters for forward-in-time upstream-biased advection schemes in ocean modeling. Mon. Weather Rev. 126, 812–830.

Rennau, H., Burchard, H., 2009. Quantitative analysis of numerically induced mixing in a coastal model application. Ocean Dyn. 59 (4), 671–687.

Shu, C.-W., 1998. Essentially non-oscillatory and weighted essentially non-oscillatory schemes for hyperbolic conservation laws. In: Advanced Numerical Approximation of Nonlinear Hyperbolic Equations. Springer, pp. 325–432.

Skyllingstad, E. D., Samelson, R. M., 2012. Baroclinic frontal instabilities and turbulent mixing in the surface boundary layer. Part I: Unforced simulations. Ocean Modell. 42, 1701–1716.

Spekreijse, S., 1987. Multigrid solution of monotone second-order discretizations of hyperbolic conservation laws. Mathematics of Computation 49 (179), 135–155.

Stone, P. H., 1966. On non-geostrophic baroclinic stability. J. Atmos. Sci. 23 (4), 390–400.

Suresh, A., Huynh, H., 1997. Accurate monotonicity-preserving schemes with Runge–Kutta time stepping. J. Comp. Phys. 136 (1), 83–99.

Sweby, 1984. High resolution schemes using flux limiters for hyperbolic conservation laws. Numerical Analysis 21, 995–1011.

Tartinville, B., Deleersnijder, E., Lazure, P., Proctor, R., Ruddick, K., Uittenbogaard, R., 1998. A coastal ocean model intercomparison study for a three-dimensional idealised test case. APM 22 (3), 165–182.

Thuburn, J., 1997. TVD schemes, positive schemes, and the universal limiter. Mon. Weather Rev. 125 (8), 1990–1993.

Umlauf, L., Lemmin, U., 2005. Inter-basin exchange and mixing in a large lake. The role of long internal waves. Limnol. Oceanogr. 50 (5), 1601–1611.

Urakawa, L., Hasumi, H., 2014. Effect of numerical diffusion on the water mass transformation in eddy-resolving models. Ocean Modell. 74, 22–35.

Vallis, G. K., 2006. Atmospheric and Oceanic Fluid Dynamics. Cambridge University Press.

van Leeuwen, S. M., van der Molen, J., Ruardij, P., Fernand, L., Jickells, T., 2013. Modelling the contribution of deep chlorophyll maxima to annual primary production in the North Sea. Biogeochemistry 113 (1-3), 137–152.

Waterson, N., Deconinck, H., 2007. Design principles for bounded higher-order convection schemes–a unified approach. J. Comp. Phys. 224 (1), 182–207.

Winters, K. B., D'Asaro, E. A., 1996. Diascalar flux and the rate of fluid mixing. J. Fluid Mech. 317 (1), 179–193.

Winters, K. B., Lombard, P. N., Riley, J. J., D'Asaro, E. A., 1995. Available potential energy and mixing in density-stratified fluids. J. Fluid Mech. 289, 115–128.

Zalesak, S. T., 1979. Fully multidimensional flux-corrected transport algorithms for fluids. J. Comp. Phys. 31 (3), 335–362.

Tables

Name	**Limiter**	**Reference**
Third Order Upwind	$\{\phi = (1/2 + x) + (1/2 - x)r, x = (1 - 2C_r)/6\}$	e.g. Pietrzak (1998)
P2-PDM	$\{\max(0, \min(\phi, 2/(1 - C_r), 2\frac{r}{C_r}))\}$	e.g. Pietrzak (1998)
Superbee	$\max[0, \min\{2r, \max(r, 1), 2\}]$	e.g. Waterson and Deconinck (2007)
SPL-$\frac{1}{3}$	$\max[0, \min(2r, 1/3 + 2r/3, 2/3 + r/3, 2)]$	e.g. Waterson and Deconinck (2007)
SPL-max-$\frac{1}{3}$	$\max[0, \min(2r, \max(1/3 + 2r/3, 2/3 + r/3), 2)]$	Waterson and Deconinck (2007)
Name	**Type**	**Reference**
MP5	Geometrical approach (monotonicity preserving, fifth order)	Suresh and Huynh (1997)
WENO	Adaptive stencil (fifth order)	e.g. Shu (1998)

Table 1: List of advection schemes. The first group of advection schemes is expressed in flux-limiter form. $r = \frac{S_{i+1} - S_i}{S_i - S_{i-1}}$, S = concentration, C_r = Courant number. In the MP5 and WENO scenarios in baroclinic instability experiment the vertical momentum and tracer advection schemes are P2-PDM. Since FOU is very diffusive, it is used just in the lateral shear instability experiment.

<table>
<tr><th colspan="7">Grid properties</th></tr>
<tr><td>Name</td><td colspan="2">R2500</td><td colspan="2">R1250</td><td colspan="2">R625</td></tr>
<tr><td>Number of cells</td><td colspan="2">96*96</td><td colspan="2">192*192</td><td colspan="2">384*384</td></tr>
<tr><td>Cell size (Δx)</td><td colspan="2">2.5 km</td><td colspan="2">1.25 km</td><td colspan="2">0.625 km</td></tr>
<tr><td>Time step (Δt)</td><td colspan="2">1.0 s</td><td colspan="2">0.5 s</td><td colspan="2">0.25 s</td></tr>
<tr><td>ND/ME0</td><td colspan="3">GaussJet</td><td colspan="3">BoxJet</td></tr>
<tr><td>Advection scheme</td><td>R2500</td><td>R1250</td><td>R625</td><td>R2500</td><td>R1250</td><td>R625</td></tr>
<tr><td>FOU</td><td>5.91×10^{-1}</td><td>5.00×10^{-1}</td><td>3.75×10^{-1}</td><td>5.91×10^{-1}</td><td>3.47×10^{-1}</td><td>2.24×10^{-1}</td></tr>
<tr><td>Third Order Upstream</td><td>4.17×10^{-2}</td><td>1.06×10^{-2}</td><td>2.80×10^{-3}</td><td>2.02×10^{-2}</td><td>7.50×10^{-3}</td><td>3.30×10^{-3}</td></tr>
<tr><td>P2-PDM</td><td>4.90×10^{-2}</td><td>1.20×10^{-2}</td><td>3.10×10^{-3}</td><td>2.41×10^{-2}</td><td>8.70×10^{-3}</td><td>3.50×10^{-3}</td></tr>
<tr><td>Superbee</td><td>-1.26×10^{-1}</td><td>-4.47×10^{-2}</td><td>-1.75×10^{-2}</td><td>-5.96×10^{-2}</td><td>-2.89×10^{-2}</td><td>-1.75×10^{-2}</td></tr>
<tr><td>SPL-max-$\frac{1}{3}$</td><td>5.70×10^{-3}</td><td>-4.60×10^{-3}</td><td>-3.00×10^{-3}</td><td>2.50×10^{-3}</td><td>-1.50×10^{-3}</td><td>-1.50×10^{-3}</td></tr>
<tr><td>SPL-$\frac{1}{3}$</td><td>1.26×10^{-1}</td><td>3.86×10^{-2}</td><td>1.19×10^{-2}</td><td>6.29×10^{-2}</td><td>2.18×10^{-2}</td><td>1.00×10^{-2}</td></tr>
<tr><td>MP5</td><td>1.89×10^{-2}</td><td>4.70×10^{-3}</td><td>1.20×10^{-3}</td><td>1.15×10^{-2}</td><td>7.80×10^{-3}</td><td>6.70×10^{-3}</td></tr>
<tr><td>WENO</td><td>3.62×10^{-2}</td><td>9.20×10^{-3}</td><td>2.60×10^{-3}</td><td>2.57×10^{-2}</td><td>1.18×10^{-2}</td><td>8.80×10^{-3}</td></tr>
</table>

Table 2: The parameters and results of the lateral shear instability test case. First panel: resolution and grid size, Second panel: The ratio of the (accumulated) global numerically dissipated energy (ND) to initial total kinetic energy (ME0) until the 8th day.

Grid properties								
Configuration	**Configuration with** $Ro = 0.8$				**Configuration with** $Ro = 0.1$			
Name	N32	N64	N128	N256	N32	N64	N128	N256
Horizontal cells number (N_x, N_y)	32*32	64*64	128*128	256*256	32*32	64*64	128*128	256*256
Horizontal grid size (Δx, km)	5.0	2.5	1.25	0.625	40.0	20.0	10.0	5.0
Barotropic time step (s)	8.0	4.0	2.0	1.0	64.0	32.0	16.0	8.0
Baroclinic time step (Δt, s)	480.0	240.0	120.0	60.0	3840.0	1920.0	960.0	480.0

Parameters			
Name	**Symbol**		
Rossby number	Ro	0.8	0.1
Velocity scale	U_0	0.2 m s^{-1}	
Coriolis frequency	f_0	$5.0 \times 10^{-5} s^{-1}$	
Rossby radius of deformation	$L_0 \approx \frac{U_0}{f_0 Ro} \approx \frac{NH}{f_0}$	5000.0 m	40000.0 m
Richardson number	$Ri = 1./Ro^2$	1.562	100
Channel width & length	$L_y \approx L_x \approx 32L_0$	160 km	1280 km
Water depth	H	200 m	1600 m
Aspect ratio	$(\delta = H/L_0)$	4.0×10^{-2}	
Vertical buoyancy gradient	$N^2 = (Lf_0/H)^2 = (f_0/\delta)^2$	$1.56 \times 10^{-6} s^{-2}$	
Horizontal buoyancy gradient	$M^2 = U/(f_0 H) = [Ro/\delta f_0^2]$	$5.0 \times 10^{-8} s^{-2}$	$6.25 \times 10^{-9} s^{-2}$

Table 3: The resolutions and parameters used in the baroclinic test case.

Name	$\Delta x = \Delta y = 1.0$ km, $\Delta z = 0.5$ m	$\Delta x = \Delta y = 0.5$ km, $\Delta z = 0.5$ m	$\Delta x = \Delta y = 1.0$ km, $\Delta z = 0.25$ m
FOU	1.0	2.74	1.406
Third Order Upwind	1.177	3.60	1.697
P2-PDM	1.27	4.0	1.81
Flux limiters	1.17	3.46	1.61
MP5	4.17	14.27	5.80
WENO	3.84	15.68	5.49

Table 4: Comparison of computational costs for the simulation of an idealised mesoscale eddy test case using different advection schemes (see the details of the test case in Klingbeil et al. (2014)). The setup is configured here as a flat bottom basin of 20 m depth and 30 km width and length. The computations are performed for three different types of computational grid configurations. The computation cost of each simulation is reported as the ratio of its computation time to the computation time of the simulation which uses the FOU advection scheme for the grid configuration with $\Delta x = 1.0$ km, and $\Delta z = 0.5$ km. All simulations are performed in serial mode.

Figures

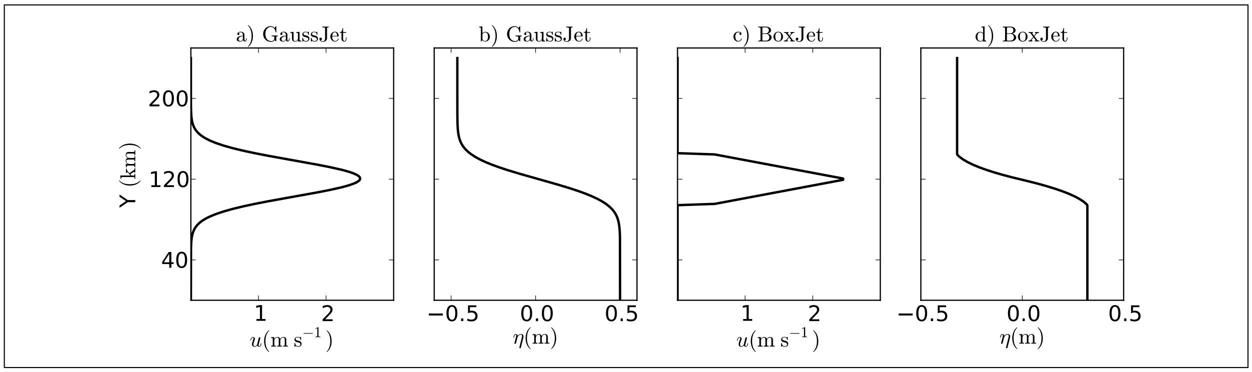

Figure 1: Initial conditions for the lateral shear instability test case. a,b : Zonal velocity and surface elevation for test GaussJet; c,d : Zonal velocity and surface elevation for test BoxJet; $u_{max} = 2.5$ m s^{-1}.

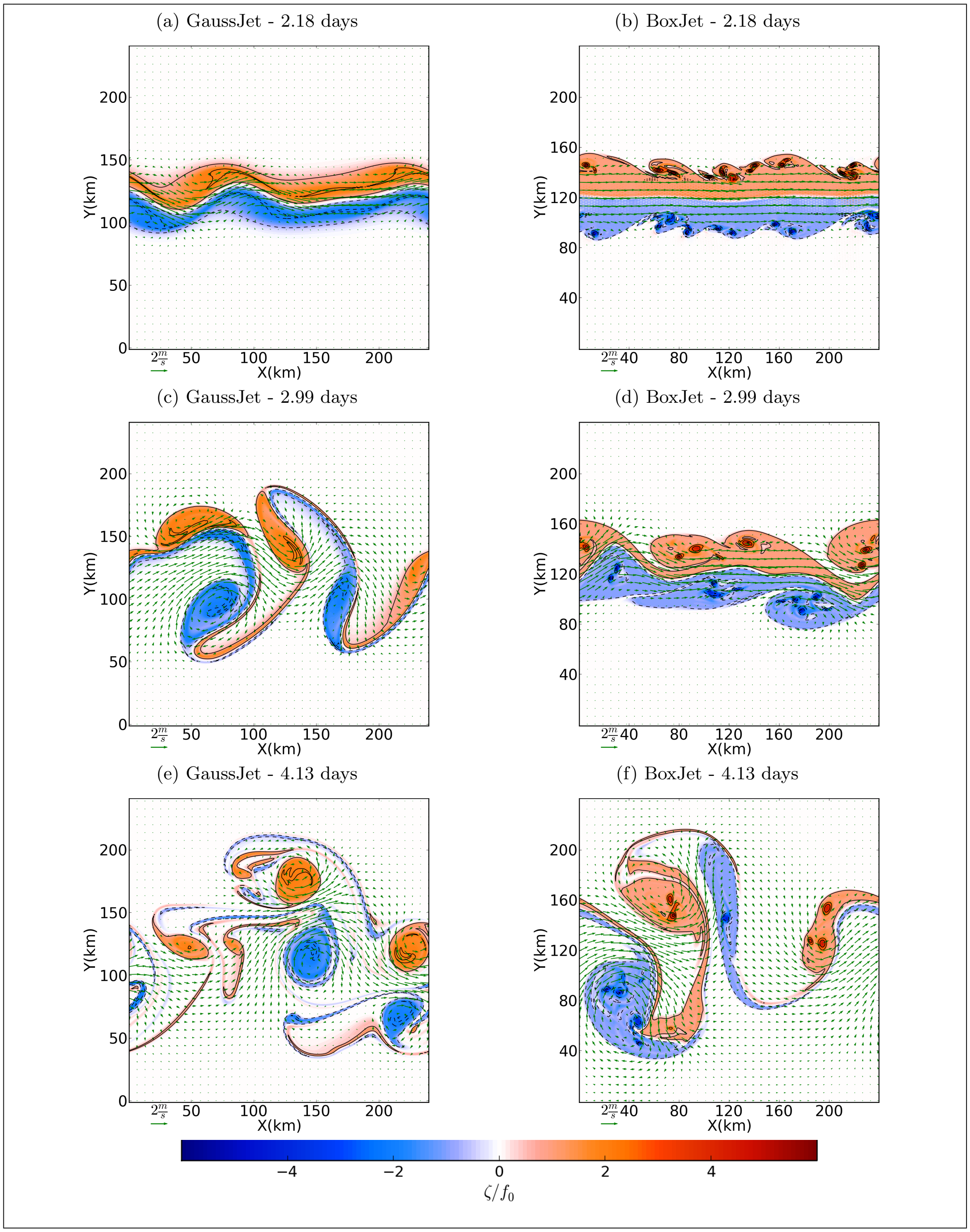

Figure 2: Time evolution of the vorticity and velocity field of GaussJet (a,c,e) and BoxJet (b,d,f) for the lateral shear instability test case using MP5 advection scheme for resolution R625.

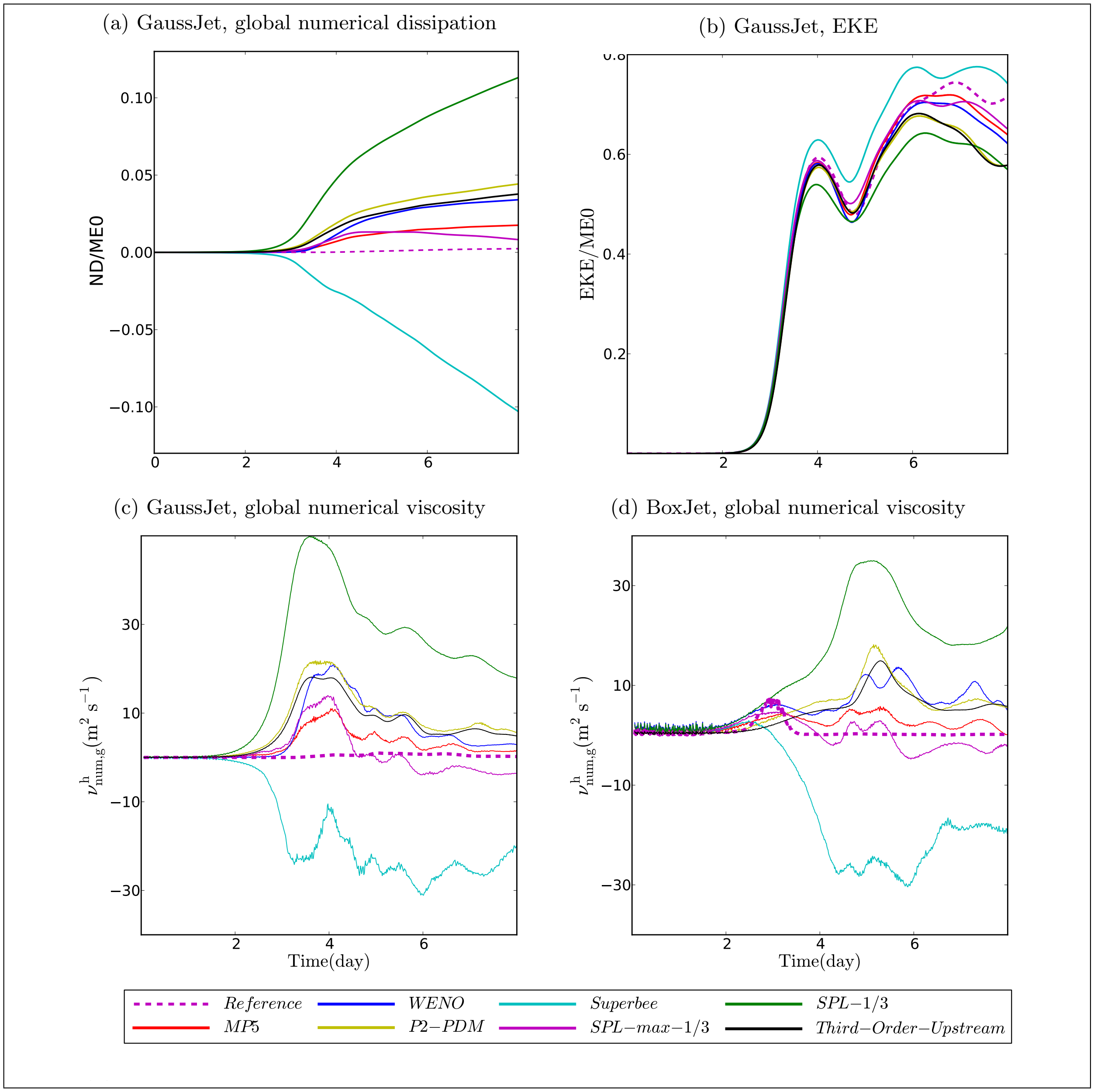

Figure 3: Lateral shear instability test case for resolution R2500: (a): ratio of (accumulated) global numerically dissipated energy to initial mechanical energy; (b): ratio of total Eddy Kinetic Energy (EKE) to total initial mechanical energy; (c,d): comparison of global numerical viscosity.

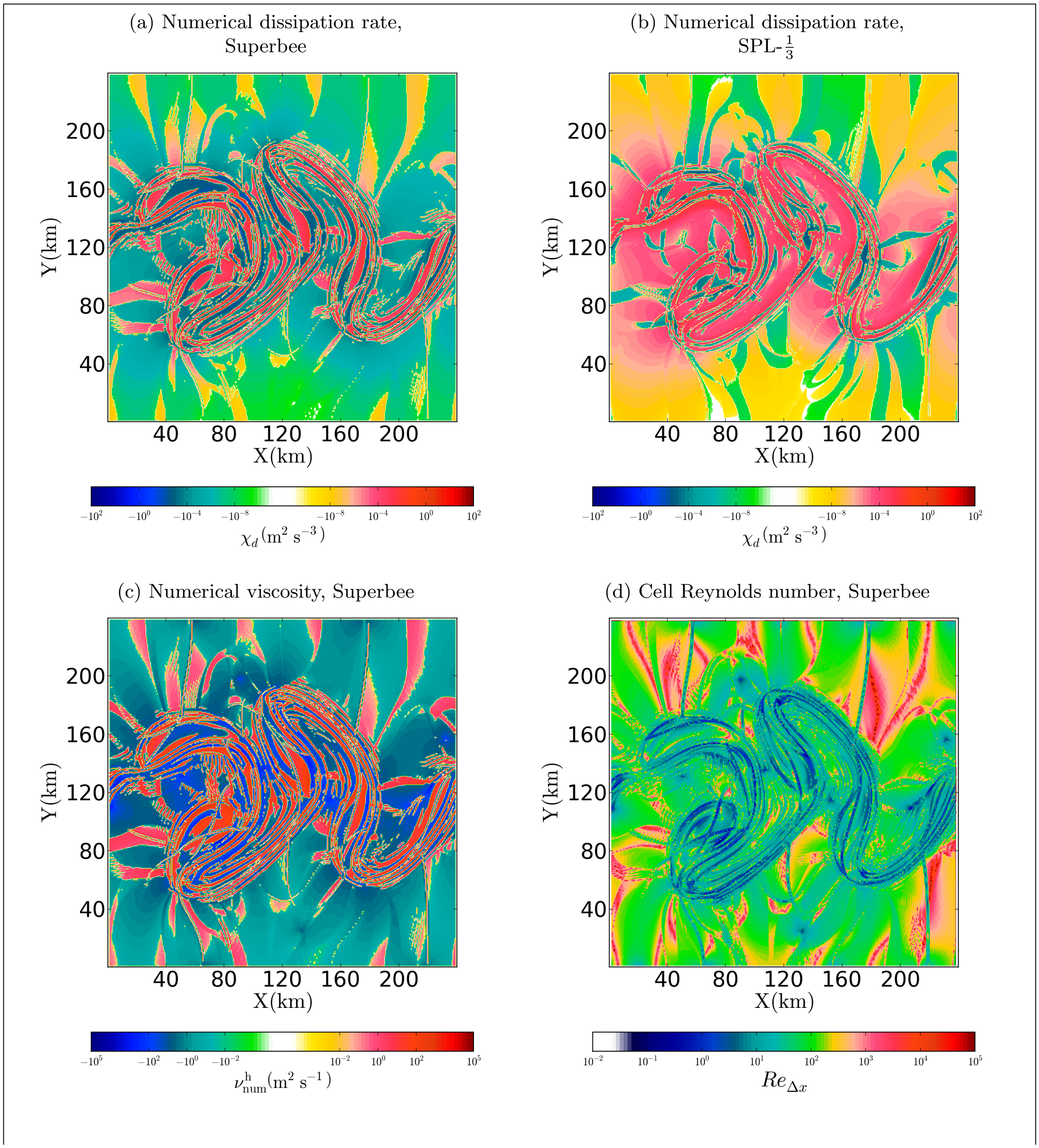

Figure 4: Lateral shear instability test case for GaussJet and the resolution R625. (a,b): Local numerical dissipation rate (see Eq. 5) for the Superbee and SPL-$\frac{1}{3}$ schemes as antidissipative and dissipative schemes, respectively. (c): Local numerical viscosity (see Eq. 11a) for the Superbee scheme. (d): Local grid Reynolds number for the Superbee scheme. All snapshots are at 2.99 days.

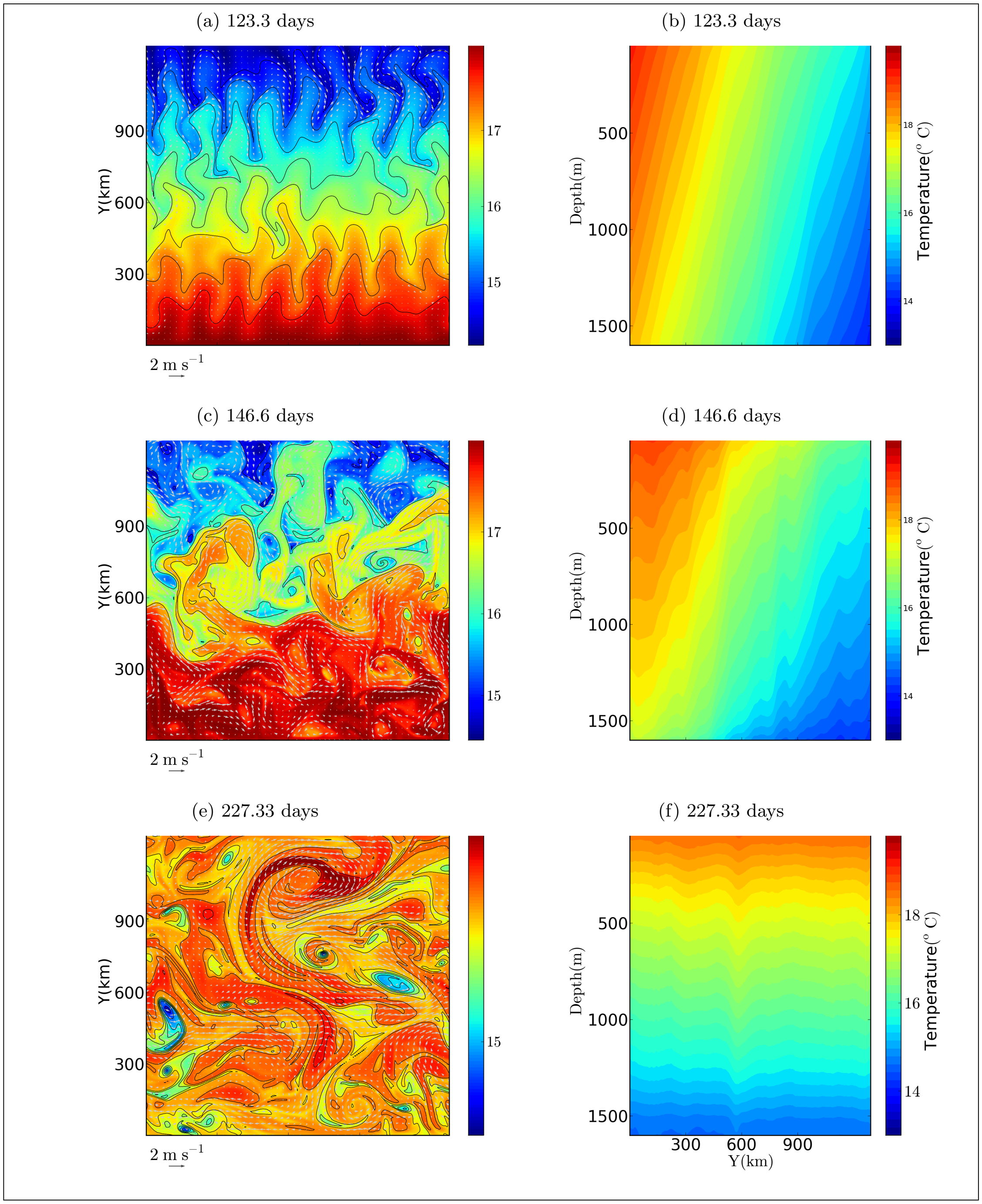

Figure 5: The configuration with $Ro = 0.1$ of baroclinic instability test case using MP5 advection scheme for the setup N256. (a,c,e): contours of horizontal surface temperature and velocity field (arrows); (b,d,f): zonal average contours of temperature.

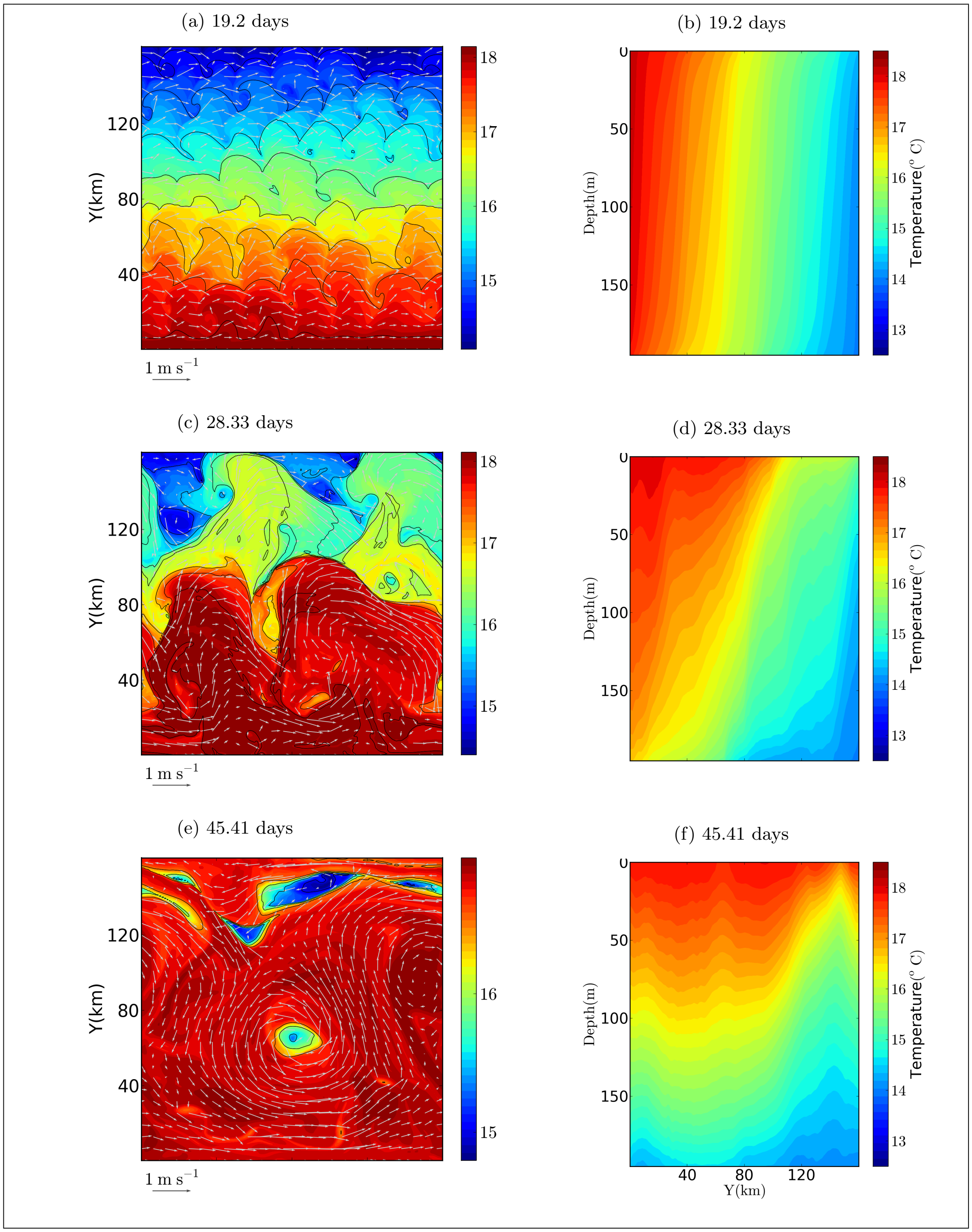

Figure 6: The configuration with $Ro = 0.8$ of baroclinic instability test case using MP5 advection scheme for the setup N256. (a,c,e): contours of horizontal surface temperature and velocity field (arrows); (b,d,f): zonal average contours of temperature.

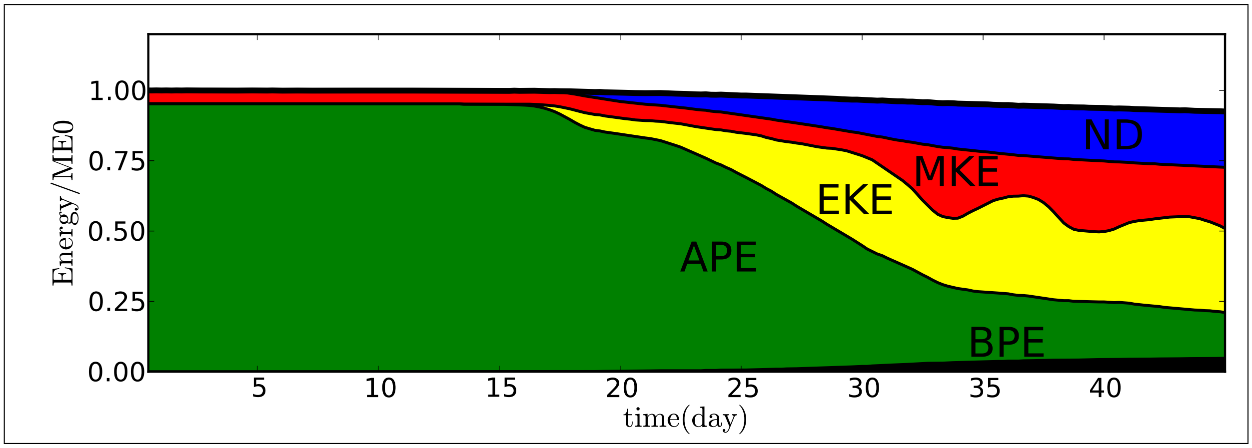

Figure 7: Evolution of the components of total energy for the baroclinic instability experiment. Stacked plots with contour shapes present the ratio of background potential energy variation (BPE), available potential energy (APE), eddy kinetic energy (EKE), mean kinetic energy (MKE) and numerical dissipation (ND) to the initial mechanical energy for the configuration with $Ro = 0.8$ using the MP5 advection scheme for the setup N128. ME0 is initial mechanical energy which is sum of initial available potential energy and initial kinetic energy. The thick black line shows the total energy level. The reduction of the total energy is due to truncation errors of other terms than the momentum advection.

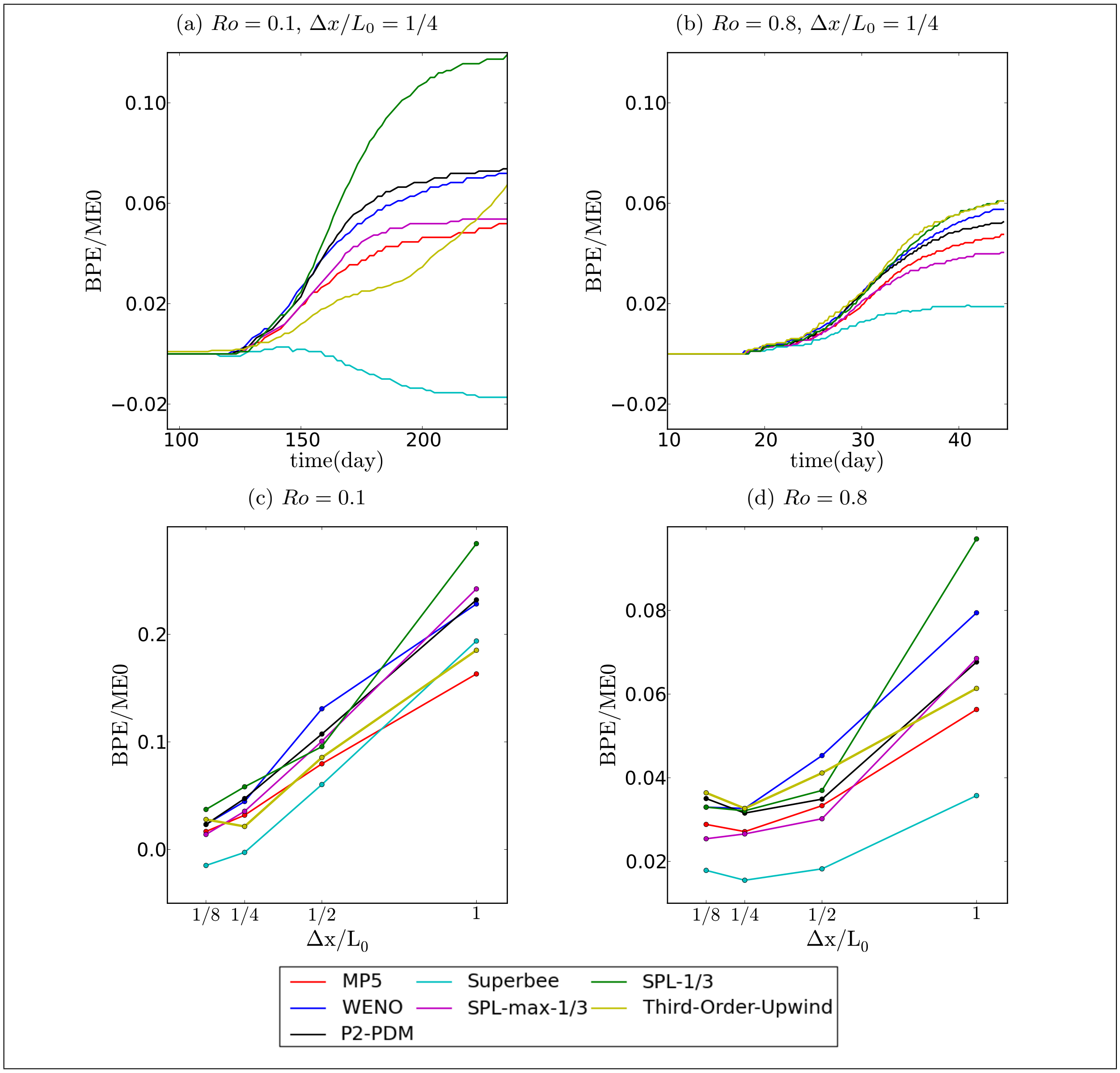

Figure 8: Baroclinic instability test case. Ratio of variation of background potential energy to initial total mechanical energy. ME0, L_0 and Δx are initial total mechanical energy, initial Rossby radius of deformation and grid size, respectively. (a,b): Time evolution of background potential energy of the configurations with $Ro = 0.1$ and the configurations with $R_0 = 0.8$ for the setup N128; (c): Background potential energy of the configuration with $Ro = 0.1$ when 70 % of available potential energy is released; (d): Background potential energy of the configuration with $Ro = 0.8$ when 65 % of available potential energy is released.

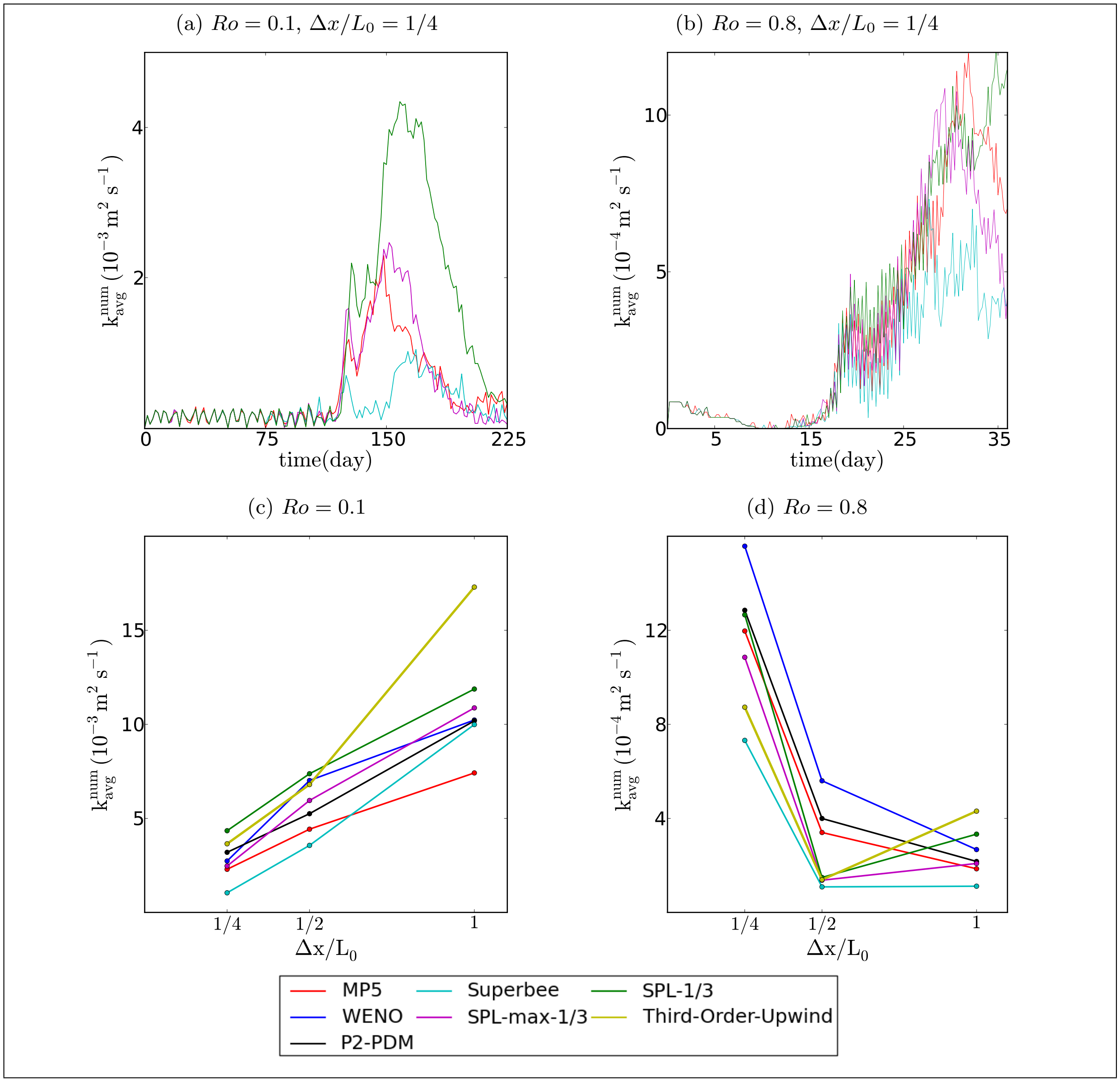

Figure 9: Baroclinic instability test case. L_0, $k_{\text{avg}}^{\text{num}}$ and Δx are initial Rossby radius of deformation, averaged numerical diapycnal diffusivity and grid size for the setup N128 for four different advection schemes (SPL-$\frac{1}{3}$, Superbee, MP5, SPL-max-$\frac{1}{3}$). (a,b): Evolution of numerical diapycnal diffusivity of the configuration with $Ro = 0.1$ and the configuration with $Ro = 0.8$; (c): maximum numerical diapycnal diffusivity of the configuration with $Ro = 0.1$; (d): maximum numerical diapycnal diffusivity of the configuration with $Ro = 0.8$.

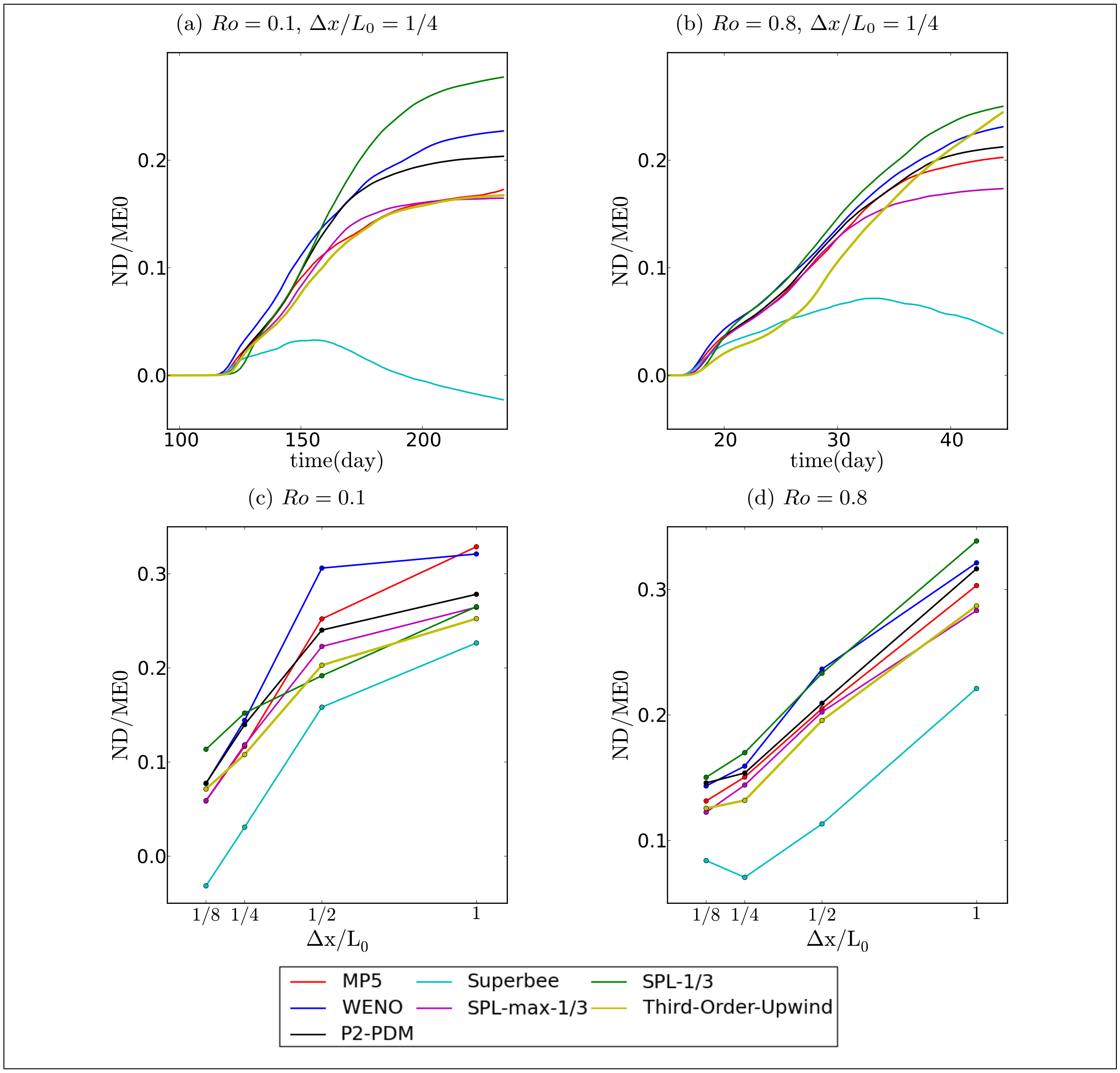

Figure 10: Baroclinic instability test case. Ratio of numerical dissipation to total initial mechanical energy. ME0, L_0 and Δx are initial total mechanical energy, initial Rossby radius of deformation and grid size. (a,b): Numerical dissipation of the configuration with $Ro = 0.1$ and the configuration with $Ro = 0.8$ for the setup N128; (c): Numerical dissipation of the configuration with $Ro = 0.1$ when approximately 70 % of available potential energy is released; (d): Numerical dissipation of the configuration with $Ro = 0.8$ when 65 % of available potential energy is released.

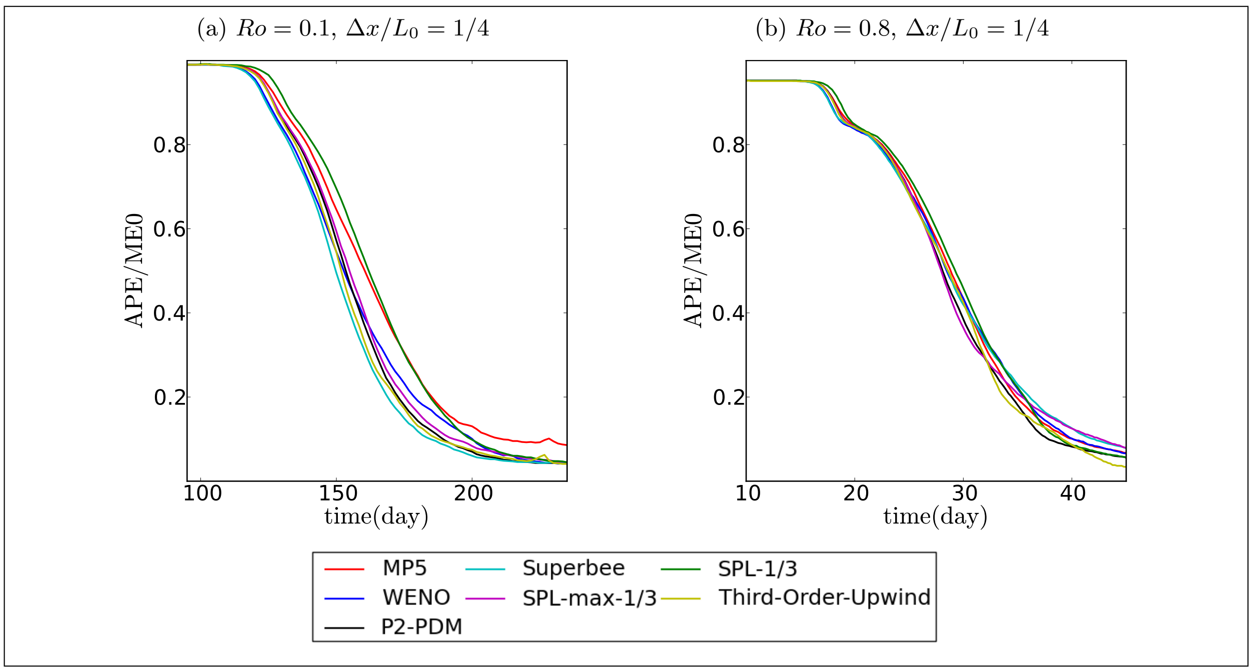

Figure 11: Baroclinic instability test case. Ratio of APE to MEO. ME0 is initial total mechanical energy. (a,b): Evolution of available potential energy of the configuration with $Ro = 0.1$ and the configuration with $Ro = 0.8$ for the setup N128.

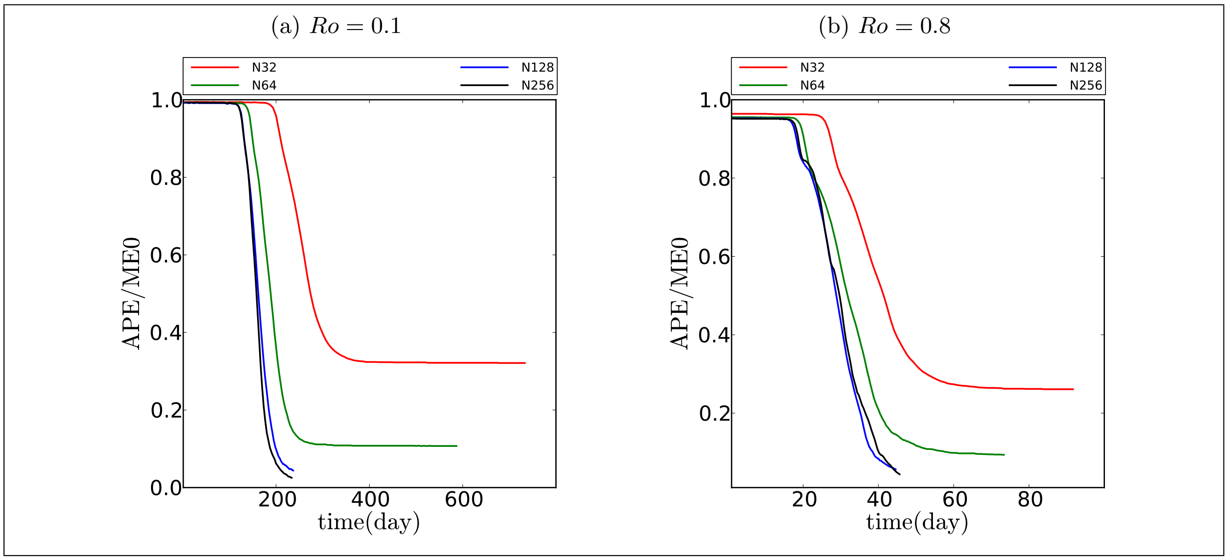

Figure 12: Baroclinic instability test case. Ratio of APE to MEO. ME0, is initial total mechanical energy. (a,b): Evolution of available potential energy of the configuration with $Ro = 0.1$ and the configuration with $Ro = 0.8$ for all resolutions using the SPL-$\frac{1}{3}$ advection scheme.

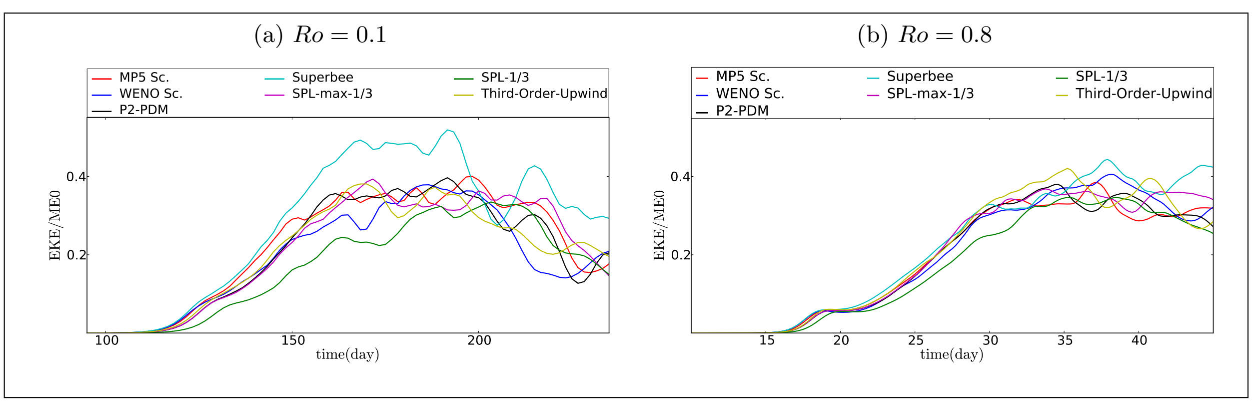

Figure 13: Baroclinic instability test case. (a,b): ratio of total Eddy Kinetic Energy (EKE) to total initial mechanical energy for the setup N128. ME0 is initial total mechanical energy.

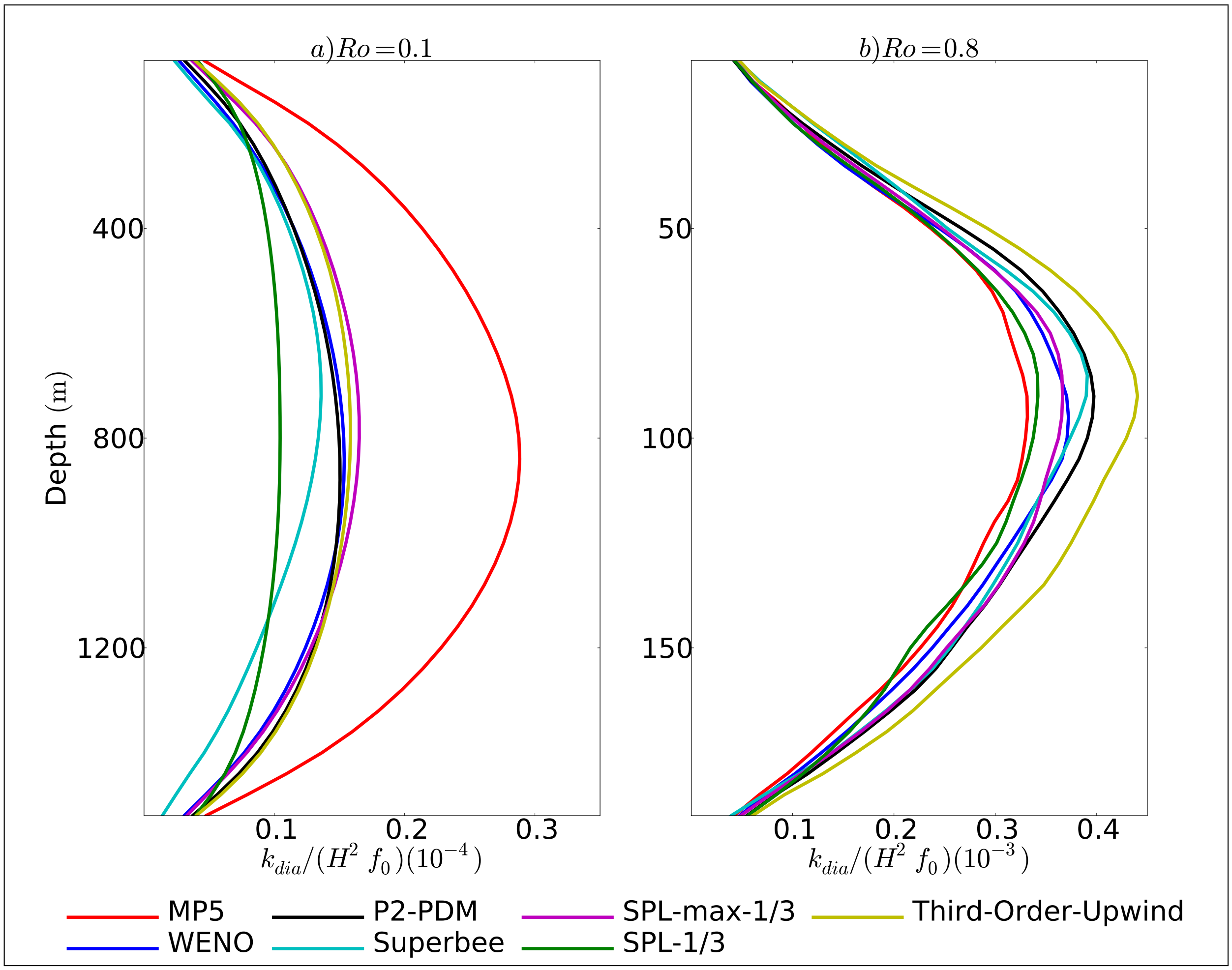

Figure 14: Baroclinic instability test case. Vertical profiles of horizontally and temporally averaged diapycnal (see Eq. 14) for the setup N128. (a): the configuration with $Ro = 0.8$, (b): the configuration with $Ro = 0.1$.